Available online at www.sciencedirect.com
SCIENCE DIRECT®
Ocean Modelling 14 (2006) 19–44
Ocean Modelling
www.elsevier.com/locate/ocemod

Parameterization of gravity current entrainment for ocean circulation models using a high-order 3D nonhydrostatic spectral element model

Xiaobiao Xu *, Yeon S. Chang, Hartmut Peters, Tamay M. Özgökmen, Eric P. Chassignet

RSMAS/MPO, University of Miami, Miami, FL 33149, United States

Received 18 July 2005; received in revised form 3 February 2006; accepted 6 February 2006
Available online 22 March 2006

Abstract

Building on the work by Turner [Turner, J.S., 1986. The development of the entrainment assumption and its application to geophysical flows. J. Fluid Mech. 173, 431–471] and Hallberg [Hallberg, R., 2000. Time integration of diapycnal diffusion and Richardson number dependent mixing in isopycnal coordinate ocean models. Mon. Weather Rev. 128, 1402–1419], an algebraic parameterization of the entrainment process in gravity current has been derived for isopycnic coordinate ocean models. It casts the entrainment into layers as a function of the layer Richardson number (Ri) times the velocity difference across layers. In order to determine the function $f(Ri)$, simulations of generic gravity currents over various bottom slope angle are conducted with the HYbrid Coordinate Ocean Model (HYCOM) and compared to similar experiments with the high-resolution, three-dimensional, nonhydrostatic model Nek5000, which serves as ground truth. A simple linear function, $E = 0.20(1 - Ri/0.25)$, is found to reproduce quite well the entrainment, salt flux, Richardson number, velocity profile and plume propagation speed in Nek5000. The parameterization is then applied to a realistic-topography simulation of the Mediterranean outflow with HYCOM and shown to produce realistic equilibration depth and water mass properties of the outflow plume.

Keywords: Parameterization; Gravity current; Entrainment; HYCOM

1. Introduction

Most deep and intermediate water masses of the world ocean are released into the large-scale circulation from high-latitude and marginal seas in the form of overflows. Examples of overflow include the Mediterranean (Baringer and Price, 1997a,b), the Denmark Strait (Girton et al., 2001; Girton and Sanford, 2003), the Faroe Bank Channel (Price, 2004), the Red Sea (Peters et al., 2005; Peters and Johns, 2005), and the Antarctic

* Corresponding author. Tel.: +1 305 421 4628.
E-mail address: xxu@rsmas.miami.edu (X. Xu).

1463-5003/$ - see front matter © 2006 Elsevier Ltd. All rights reserved.
doi:10.1016/j.ocemod.2006.02.006

slope plumes in the margin of the Antarctic Ocean (Gordon et al., 2004). The entrainment of ambient waters into overflows is a key process determining the water properties and volume transports of the outflow product water. It thus has high impact on the ocean general circulation and the earth's climate, and oceanic general circulation models (OGCMs) are quite sensitive to overflow representation (e.g., Willebrand et al., 2001), the topic of the "Gravity Current Entrainment Climate Process Team" (http://www.cpt-gce.org/).

Parameterizing the gravity current entrainment in coarse-resolution OGCMs and climate models is challenging. Recent simulations of the Mediterranean overflow employing isopycnic coordinates (Papadakis et al., 2003) and terrain-following coordinates (Jungclaus and Mellor, 2000) appear promising, while the representation of continuous slopes as steps in geopotential vertical coordinate models remains a daunting problem (e.g., Beckmann and Döscher, 1997; Winton et al., 1998; Killworth and Edwards, 1999; Nakano and Suginohara, 2002). In this paper, we exclusively focus on entrainment parameterizations in isopycnic coordinate models, which have a vertical coordinate system that naturally migrates to the density front atop the gravity current, where most of the entrainment takes place. Isopycnic models do not suffer from numerically induced diapycnal mixing (Griffies et al., 2000), and thus the entrainment can be finely controlled. Given the potential applications in climate models, we consider in this study only algebraic (diagnostic) parameterization schemes and deliberately ignore the more complex (prognostic), two-equation turbulence closure models (e.g., Jungclaus and Mellor, 2000; Ezer and Mellor, 2004).

A common approach to describe the entrainment in stratified shear flows is in relation to a Richardson number (Fernando, 1991, Table 1). One example is the widely used K-Profile Parameterization (KPP hereafter) developed by Large et al. (1994, 1997) and Large (1998). In KPP, the mixing in the ocean interior due to shear instability is parameterized by

$$K = K_{\max}\left[1 - \min(1, Ri/Ri_{\mathrm{c}})^2\right]^3, \tag{1}$$

where K is the vertical diffusivity or viscosity, and Ri is the shear Richardson number, defined as

$$Ri = N^2\left[\left(\frac{\partial u}{\partial z}\right)^2 + \left(\frac{\partial v}{\partial z}\right)^2\right]^{-1}, \tag{2}$$

where the numerator and the denominator are the square of buoyancy frequency and vertical shear, respectively. There are two constants in Eq. (1), the maximum diffusivity $K_{\max} = 5.0 \times 10^{-3}\ \mathrm{m}^2\,\mathrm{s}^{-1}$ and the cut-off Richardson number $Ri_{\mathrm{c}} = 0.7$. The values are derived from large eddy simulations (LES) of the upper tropical ocean (Wang et al., 1996, 1998; Large and Gent, 1999). KPP is not valid universally since it does not conform to the Buckingham's Pi-theorem (e.g., Kundu, 1990) which states that constants in a physical law should be dimensionless. Diffusivity values significantly larger than the above $K_{\max}$ have been indeed observed in the equatorial Pacific Ocean (e.g., Peters et al., 1988).

Another example is the bulk entrainment parameterization of Turner (1986) (TP hereafter) which was applied to isopycnic coordinate models by Hallberg (2000) and used by Papadakis et al. (2003). In the original TP, the entrainment velocity w_{E} into the gravity current is specified as

$$w_{\mathrm{E}} = \Delta U \frac{0.08 - 0.1Ri_{\mathrm{B}}}{1 + 5Ri_{\mathrm{B}}} \tag{3}$$

for $0 \leqslant Ri \leqslant 0.8$ and $w_{\mathrm{E}} = 0$ for $Ri > 0.8$. Ri_{B} in Eq. (3) is the bulk Richardson number, defined as

$$Ri_{\mathrm{B}} = \frac{\Delta\rho g h}{\rho\Delta U^2}, \tag{4}$$

where h is the thickness of the gravity current plume, ΔU and $\Delta\rho$ are the velocity and density difference between the gravity current and environment water. Eq. (3) is based on laboratory experiments of entraining gravity currents by Ellison and Turner (1959) and the subsequential analysis by Turner (1986). One may question how well these laboratory results are representative of the real ocean. Price and Baringer (1994) were, however, able to successfully predict the water property change in four observed outflow cases using Eq.

(3) in a one-dimensional stream tube model: the Mediterranean outflow, the Denmark Strait and Faroe Bank Channel outflow from the Nordic Seas and the Filchner ice shelf outflow into the Weddell Sea.

As it is notoriously difficult to quantitatively compare model simulations with oceanic observations, we follow Chang et al. (2005) in resorting to a model-to-model comparison in similar, generic flow scenarios. Chang et al. (2005) compared KPP and TP in an idealized gravity current scenario with the hydrostatic HYbrid Coordinate Ocean Model (HYCOM). They found that the gravity current entrainment resulting from KPP and TP differs significantly from one another. Compared to the output of a high-order three-dimensional (3D) nonhydrostatic spectral element model Nek5000 (Fischer, 1997), the entrainment specified by KPP was too weak while that from TP was too strong. They further calibrated the parameters of both schemes based on Nek5000 results. Another important result from Chang et al. (2005) is that the hard limitation of the eddy diffusivity in KPP by $K_{\max}$ does not allow for an adjustment of the strength of mixing with different forcing beyond $K_{\max}$, while such an adjustment is given in TP through the dependence of w_E on ΔU. Furthermore, in a set of numerical experiments with varying sea floor slopes, the entrainment remained constant in KPP, but increased in proportion to the slope angle in TP. Thus, Chang et al. (2005) concluded that the TP approach is more adequate for gravity current mixing parameterization.

An assumption underlying the concept of entrainment in Turner (1986) is that the entire gravity current is viewed as a single layer, thus ΔU and Ri_B in Eq. (3) are the 'bulk' properties averaged over the cross-section of a stream-tube. The entrainment modifies the water properties throughout the layer in the descending plume. In isopycnic coordinate models, multiple layers are needed to properly represent the gravity current. Hallberg (2000) therefore defined a layer Richardson number Ri_k (his Eq. (5.3))

$$Ri_k = \frac{\Delta\rho_k g h_k}{\rho_k \Delta U_k^2}, \tag{5}$$

in which

$$\frac{\Delta\rho_k}{\Delta U_k^2} = 2\left(\frac{|\mathbf{u}_k - \mathbf{u}_{k-1}|^2}{\rho_k - \rho_{k-1}} + \frac{|\mathbf{u}_k - \mathbf{u}_{k+1}|^2}{\rho_k - \rho_{k+1}}\right)^{-1}. \tag{6}$$

Here, h, ρ, and $\mathbf{u}$ represent the thickness, density and horizontal velocity, and the subscripts are layer indexes. Hallberg (2000) then implemented Eq. (3) in each layer using the layer Richardson number. This raises an issue as to whether the local layer Ri_ks are able to represent the bulk Ri_B. Specifically, the real skill of an isopycnic model in representing gravity current lies in the ability to migrate its resolution to the interface between the gravity current and ambient water above. Thus, the layer Ri_k effectively becomes the shear Ri as defined by Eq. (2) and this leaves the implementation of Eq. (3) without a solid experimental foundation.

In this paper, we develop an entrainment parameterization of the form

$$E \equiv \frac{w_E}{\Delta U} = f(Ri), \tag{7}$$

in which Ri is the local layer Richardson number as defined above. We maintain a TP-like structure and keep ΔU as a relevant scale for w_E because, physically, the turbulence produced due to interfacial shear is the dominant energy source for mixing (Narimousa and Fernando, 1987). Our approach to determine $f(Ri)$ is experimental. First, a number of simple linear functions are employed in HYCOM in a generic gravity current configuration tailored to match similar simulation with the nonhydrostatic model Nek5000, which serves as our ground truth. Based on these results, we then develop an optimized formula and evaluate its performance in similar configurations with various forcing. Finally, to briefly explore if this optimized parameterization leads to reasonable results for realistic oceanic overflows as well, we conduct a HYCOM experiment of the Mediterranean overflow and compare the simulated equilibrium depth of the salinity tongue to observations. This is a simple but efficient test since the simulated Mediterranean outflow plume would settle down either too deep or too shallow in the Gulf of Cadiz if the entrainment were under- or over-prescribed.

The paper is organized as follows. The nonhydrostatic model Nek5000 and the hydrostatic oceanic general circulation model (OGCM) HYCOM are introduced in Section 2, followed by the experimental setups and the model parameters in Section 3. The development of an optimized parameterization following (7) is laid out in

Section 4. The new scheme is then applied to the Mediterranean outflow and described in Section 5. Finally, the main findings are summarized and discussed in Section 6.

2. The numerical models

The hydrostatic OGCM used in this study, HYCOM, is discussed in Bleck (2002), Chassignet et al. (2003), and Halliwell (2004). A detailed documentation is available on-line at http://www.hycom.org. Gravity current simulations with HYCOM in isopycnic mode have been reported by Papadakis et al. (2003) and Chang et al. (2005).

As our ground truth, we use high-resolution simulations with the nonhydrostatic spectral element Navier Stokes solver Nek5000. This model is documented in detail by Fischer (1997), Fischer et al. (2000), Tufo and Fischer (1999), and Fischer and Mullen (2001). The application to studies of bottom gravity currents is discussed in detail in Özgökmen et al. (2004a,b, 2006) and Chang et al. (2005), and thus needs no further introduction.

3. Experimental configuration

The Nek5000 channel-like model domain has a horizontal, streamwise length of $L_x = 10$ km and a spanwise width of $L_y = 2$ km. The depth of the water column at the inlet ($x = 0$) is $h_i = 400$ m. The maximum depth can reach $H = 1000$ m depending on the geometry dictated by constant slope angles of $\theta = 1°$, 2°, 3°, and 4°. The boundary conditions at the bottom are no-slip and no-normal flow for velocity, and no-normal flux for salinity, $\partial S/\partial \mathbf{n} = 0$, where $\mathbf{n}$ is normal to the boundary. Rigid-lid and free-slip boundary conditions are used at the top. The model is initialized by placing a salty and thus dense water mass at the top of the slope and driven by specifying velocity and salinity profiles at the inlet boundary. Periodic boundary conditions are applied at the channel sides. The domain is discretized using 4000 elements with sixth-order polynomials in each spatial direction within the elements, hence a total of 864,000 grid points are employed. The remaining model parameters are listed in Table 1 and the reader is referred to Özgökmen et al. (2004a) and Chang et al. (2005) for further detail. The calculations were carried out on a Linux cluster running on 32 Athlon 1.7 GHz processors.

The configuration of HYCOM experiments is set up to closely mimic that of Nek5000. The computational domain has a 20 km long, 2 km wide sloping bottom with the same angles as in Nek5000. A horizontal resolution of 100 m is used in all experiments. There are totally seven layers in vertical: a thin (10 m) mixed layer on top and six isopycnic layer corresponding to salinity anomaly of 0.0, 0.2, 0.4, 0.6, 0.8, and 0.9 psu. The initial condition consists of dense saline water over the first 1 km of the slope as in the Nek5000. In a 1 km long relaxation zone of 400 m constant depth, the salinity and velocity profiles are relaxed to the Nek5000 profiles (Fig. 1).

Table 1
Parameters of the Nek5000 nonhydrostatic model simulations

Domain size (L_x, $L_z = H$, L_y)	(10 km, 1 km, 2 km)
Bottom slope (θ)	1°, 2°, 3°, 4°
Rayleigh number (Ra)	5×10^6
Prandtl number (Pr)	1
Ratio of vertical to horizontal eddy viscosity (r)	2×10^{-2}
Salinity range (S)	1.0 psu
Number of elements (x, z, y)	50, 8, 10
Polynomial degree (N)	6
Number of grid points	864,000
Time step (Δt)	0.85 s

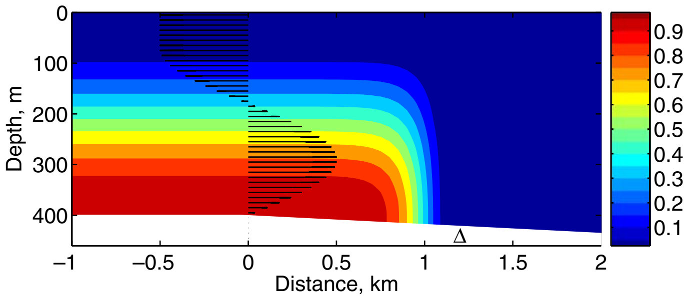

Fig. 1. The initial distribution of the salinity anomaly and the velocity profile in the relaxation zone ($x = -1$ to $x = 0$ km) in the HYCOM configuration. $X_0 = 1.2$ km is marked as a $\triangle$.

4. Results

4.1. Results from the nonhydrostatic 3D model

The evolution of the salinity distribution in Nek5000 experiments is shown in Fig. 2. The basic characteristics of such a flow field have been described and quantified in Özgökmen et al. (2004a), to which we refer the reader for further detail. Fig. 2 clearly demonstrates that, as the slope angle increases, the turbulent overturning structures between the gravity current and ambient fluid become larger and more vigorous, an indication of enhanced mixing and entrainment.

In order to average over the 3D mixing structures, a spanwise-averaged length, or propagation distance of the gravity current, $\ell(t)$, is defined as

$$\ell(t) = L_y^{-1} \int_0^{L_y} X_{\mathrm{F}}(y', t)\mathrm{d}y' - X_0. \tag{8}$$

Here, $X_0 = 1.2$ km is a reference location immediately downstream of the dense water pool at the top of the slope before any entrainment occurs in Nek5000 or HYCOM, and $X_{\mathrm{F}}(y, t)$ represents the leading edge of the plume. Its propagation speed is then defined as

$$U_{\mathrm{F}}(t) = \mathrm{d}\ell(t)/\mathrm{d}t. \tag{9}$$

In the time evolution of ℓ and U_{F} (Fig. 3), the modeled gravity currents quickly attain a nearly constant speed of propagation for all slope angles. This property is well known from lock-exchange flows (e.g., Keulegan, 1958) and constant-flux gravity currents (e.g., Ellison and Turner, 1959; Britter and Linden, 1980). The propagation speed is insensitive to variations in slope angle for large θ since the increase in buoyancy force resulting from a greater slope angle is approximately compensated by the buoyancy gain from increased entrainment. Fig. 3 shows that there is approximately a 20% variation in U_{F} over the range of slope angles from $\theta = 1°$ to 4°, which can be explained by the greater effect of the bottom friction at small slopes (Britter and Linden, 1980). With increasing θ, the corresponding change in U_{F} becomes increasingly smaller (Fig. 3).

The comparison of the Nek5000 and HYCOM simulations is quantified by an entrainment parameter $\mathscr{E}$ and a volume-averaged salt flux F_{S}. Turner (1986) defined the entrainment $\mathscr{E}$ as the change of the plume thickness h in the streamwise direction X:

$$\mathscr{E} \equiv \frac{\mathrm{d}h}{\mathrm{d}X}. \tag{10}$$

Following Özgökmen et al. (2004a), a two-dimensional (2D) expression which can be mapped to 3D flows is

$$\mathscr{E}(t) \equiv \frac{\overline{h}(t) - \overline{h}_0(t)}{\ell(t)}, \tag{11}$$

where $\overline{h}(t)$ is the mean thickness between the reference location X_0 and the leading edge of the density current X_{F},

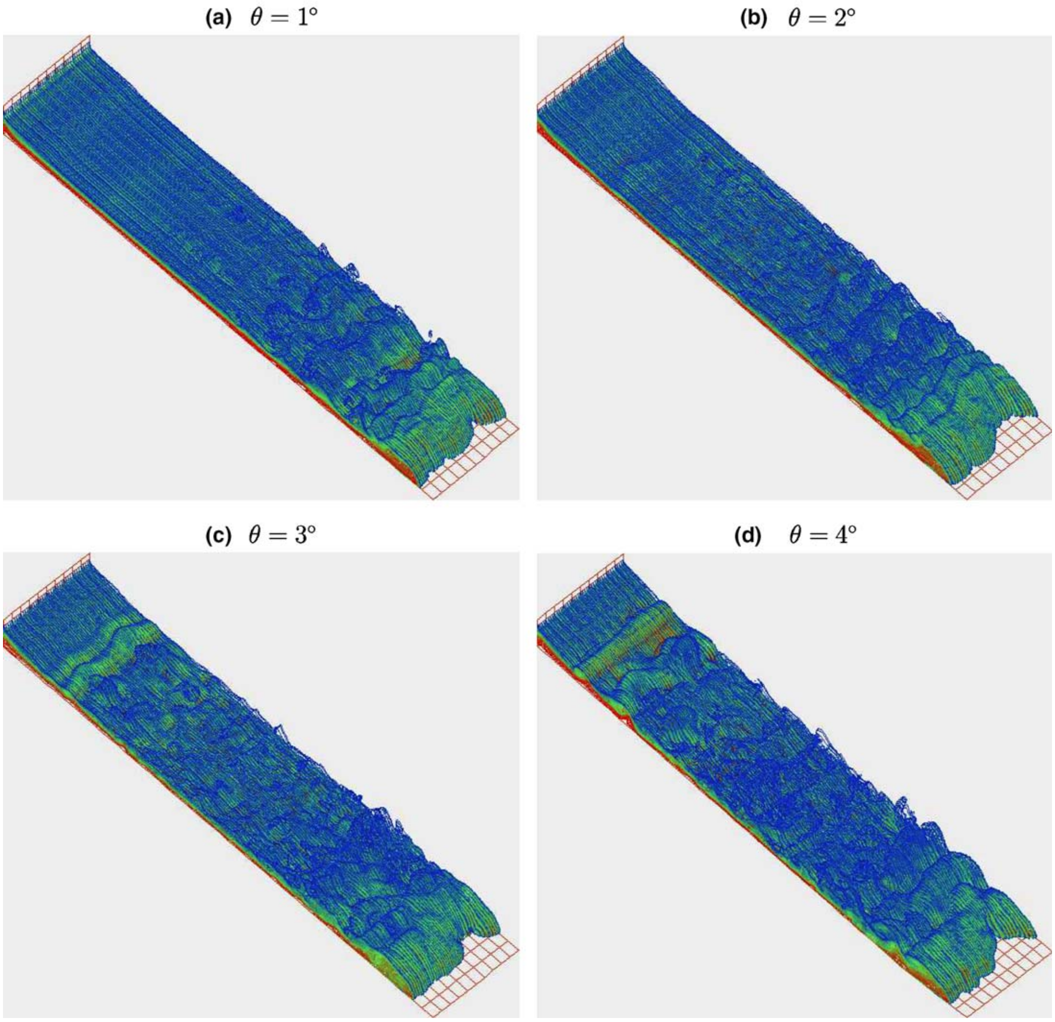

Fig. 2. Snapshots of the salinity anomaly distribution in Nek5000 experiments with four different slope angles when the gravity current reaches the end of the domain.

$$\overline{h}(t) \equiv \frac{1}{\ell(t)\ L_y} \int_0^{L_y} \int_{X_0}^{X_\mathrm{F}(y,t)} h(x',y',t)\mathrm{d}x'\ \mathrm{d}y'. \tag{12}$$

The gravity current thickness h in (12) is defined as

$$h(x,y,t) \equiv \int_0^{z^b} \delta(x,y,z',t)\mathrm{d}z', \quad \text{where } \delta = \begin{cases} 0, & \text{if } S'(x,y,z,t) < \epsilon \\ 1, & \text{if } S'(x,y,z,t) \geqslant \epsilon \end{cases}. \tag{13}$$

S' in Eq. (13) is the salinity anomaly and the top of plume is taken to be $\epsilon = 0.2$ psu surface since it delineates the coherent part of the gravity current in the Nek5000 simulations. Fluid particles with lower salinity tend to be detached from the current and to be advected with the overlying counter flow. Finally, $\overline{h}_0(t)$ in (11) is the mean thickness between X_0 and X_F when there is no entrainment. It is physically equivalent to the volume passing X_0 divided by the distance $\ell(t)$ and spanwise width L_y:

$$\overline{h}_0(t) \equiv \frac{1}{\ell(t)L_y} \int_0^{t} \int_0^{L_y} \int_{z^b+h}^{z^b} u(X_0,y',z',t')\mathrm{d}z'\ \mathrm{d}y'\ \mathrm{d}t'. \tag{14}$$

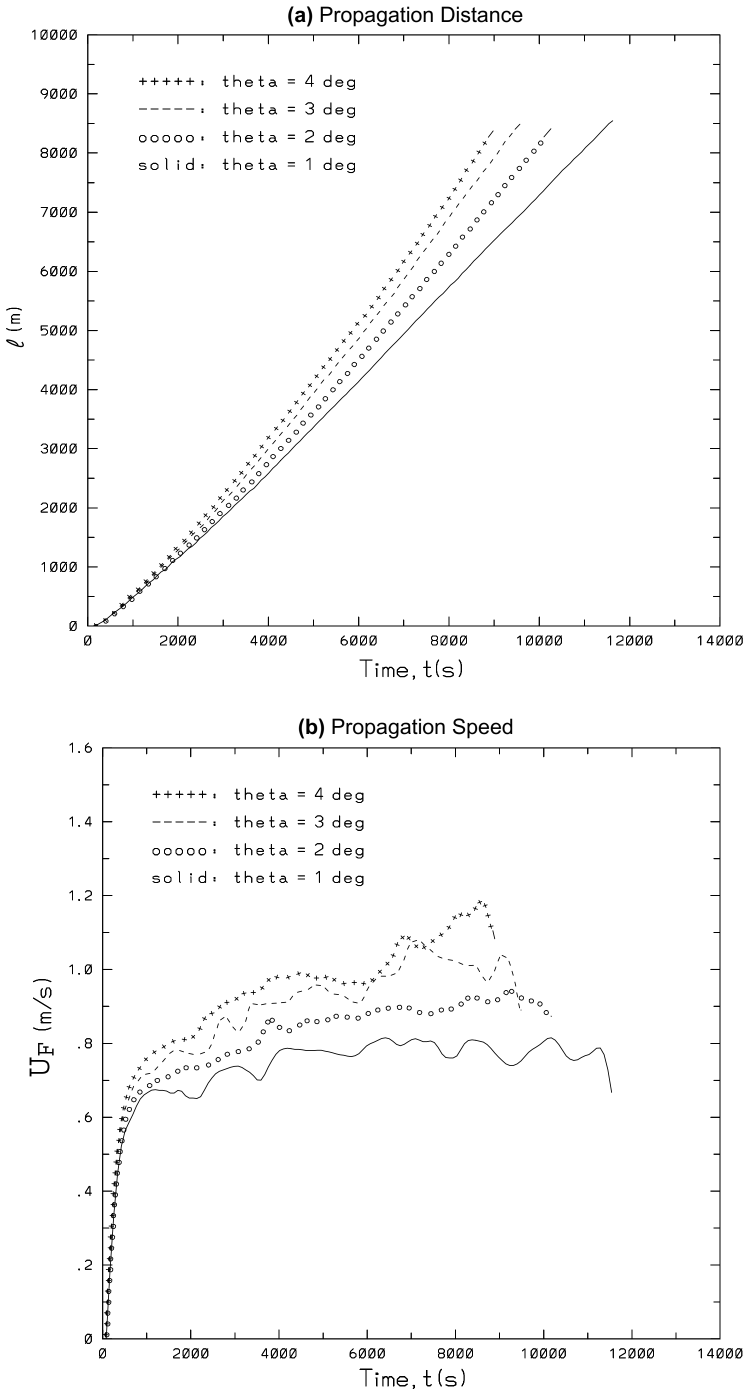

Fig. 3. (a) Propagation distance ℓ in m and (b) propagation speed U_F in m s^{-1} of the gravity currents as a function of time in Nek5000 experiments with four slope angles.

The volume-averaged salt flux F_S (kg m^{-2} s^{-1}) is defined as

$$F_S(t) \equiv \frac{1}{\overline{X_F}(t)L_y h_0}\int_0^{X_F(y,t)}\int_0^{L_y}\int_{z^b+h}^{z^b}\rho\frac{S'(x',y',z',t)}{1000}u(x',y',z',t)\mathrm{d}z'\ \mathrm{d}y'\ \mathrm{d}x', \tag{15}$$

where S', h, and L_y, are the salinity anomaly, gravity current thickness and spanwise width, respectively. $\overline{X_F}$ is the spanwise-averaged position of the gravity current edge, or X_F, and $h_0 = 200$ m is the initial plume thickness.

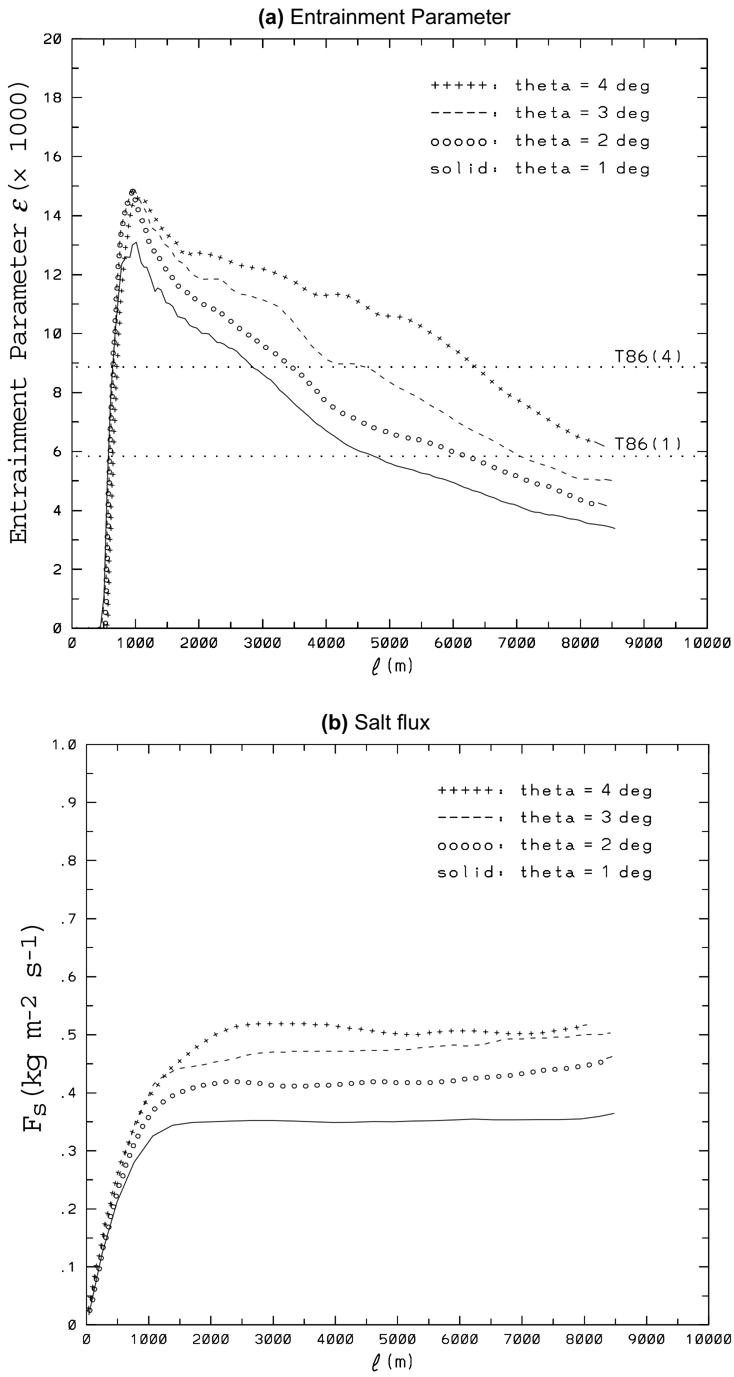

Fig. 4. (a) Entrainment parameter $\mathscr{E}$ and (b) salt flux F_S in kg m^{-2} s^{-1} as a function of the gravity current length ℓ in Nek5000 experiments with four different bottom slopes. The dotted lines in (a) mark the values of $\mathscr{E}$ corresponding to $\theta = 1°$ and $\theta = 4°$ in the formula $\mathscr{E} = 10^{-3} \times (5 + \theta)$ of Turner (1986).

Fig. 4 shows the evolution of entrainment parameter $\mathscr{E}$ and salt flux F_S as function of plume propagation distance ℓ from the Nek5000 runs. For all four runs, the entrainment parameter consistently decays with distance after initial transients (Fig. 4a). Similar results are found in Özgökmen et al. (2004a) and Chang et al. (2005). We choose to present the evolution as function of distance $\ell(t)$ rather than time in order to allow for

Table 2
Values of E_0 in experiment sets A, B, C, and D

#	Exp. A ($Ri_c = 0.75$)	Exp. B ($Ri_c = 0.50$)	Exp. C ($Ri_c = 0.35$)	Exp. D ($Ri_c = 0.25$)
1	0.0025	0.0025	0.0025	0.01
2	0.01	0.01	0.01	0.04
3	0.02	0.02	0.03	0.08
4	0.03	0.04	0.05	0.12
5	0.04	0.06	0.08	0.20
6	0.06	0.08	0.12	1.00

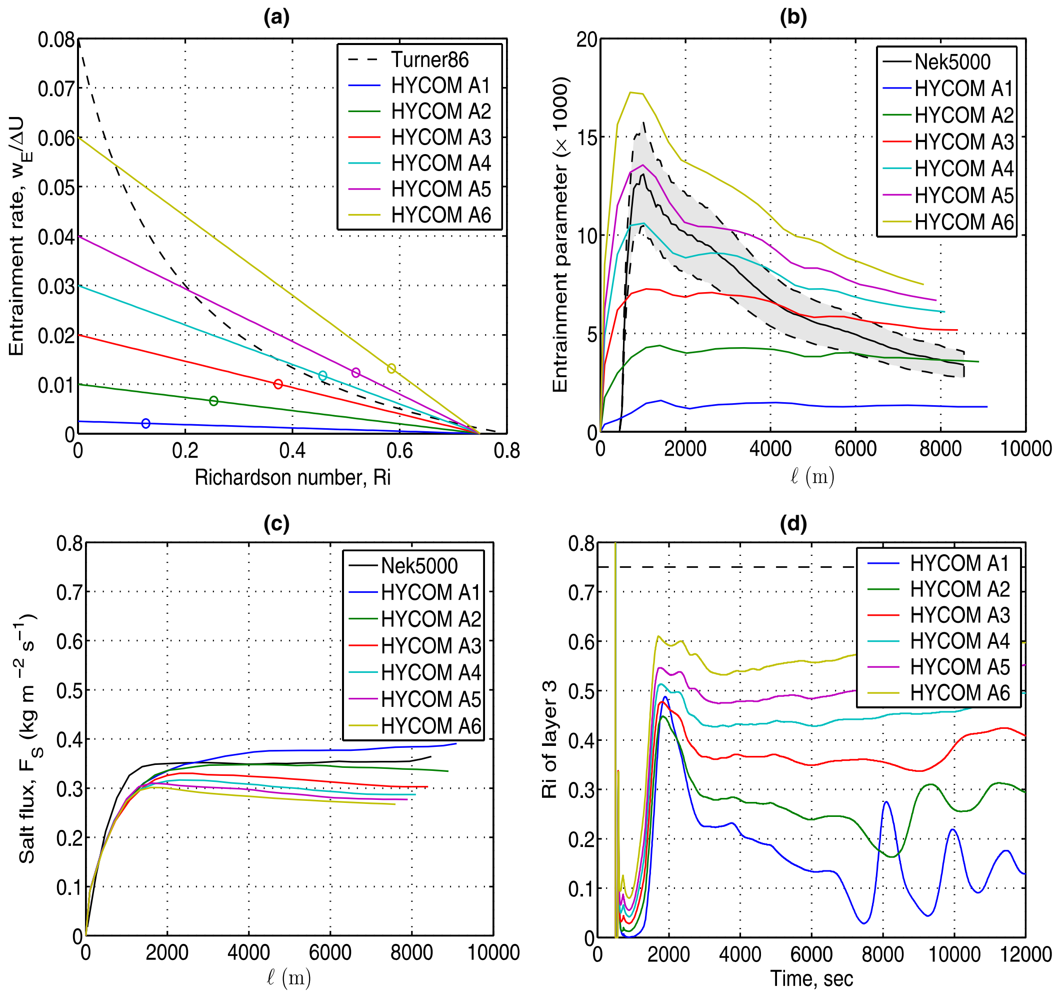

Fig. 5. Results from Exp. A, $Ri_c = 0.75$. (a) Entrainment rate E as linear functions of Ri in experiments A1–A6. The dash line is Turner's (1986) formula (3). The time-averaged Ri of layer 3 is marked as "○". (b) Entrainment parameter $\mathscr{E}(\ell)$ from Nek5000 and HYCOM. The shaded area represents a ±20% variance around Nek5000 results. (c) Salt flux $F_S(\ell)$ in kg m^{-2} s^{-1} from HYCOM in comparison to Nek5000. (d) Richardson number $Ri(t)$ of layer 3 at $x = X_0$ from HYCOM experiments, with the dash line marks Ri_c.

the same development in mixing along the plume path. As expected, $\mathscr{E}(\ell)$ increases with increasing bottom slope θ, with the variation magnitude comparable to Turner's (1986) formula $\mathscr{E} = 10^{-3} \times (5 + \theta)$. The salt flux $F_S(\ell)$ reaches an equilibrium values shortly after the initial descent of the gravity currents (Fig. 4b). The variations in S_F for different θ are due to the different gravity current velocities and entrainment characteristics as well.

4.2. HYCOM with linear parameterization functions $E = f(Ri)$

In order to keep the parameterization functions as simple as possible, we experiment with linear functions of the form:

$$E = \begin{cases} E_0\left(1 - \frac{Ri}{Ri_c}\right), & \text{when } 0 \leqslant Ri < Ri_c \\ 0, & \text{when } Ri \geqslant Ri_c. \end{cases} \tag{16}$$

Since both of E_0 and Ri_c are unknown, our first step is to investigate the effect of varying these two parameters: increasing E_0 means a larger magnitude of the entrainment, while increasing Ri_c implies that the gravity current can entrain over a wider range of flow conditions. Different combinations of E_0 and Ri_c might produce

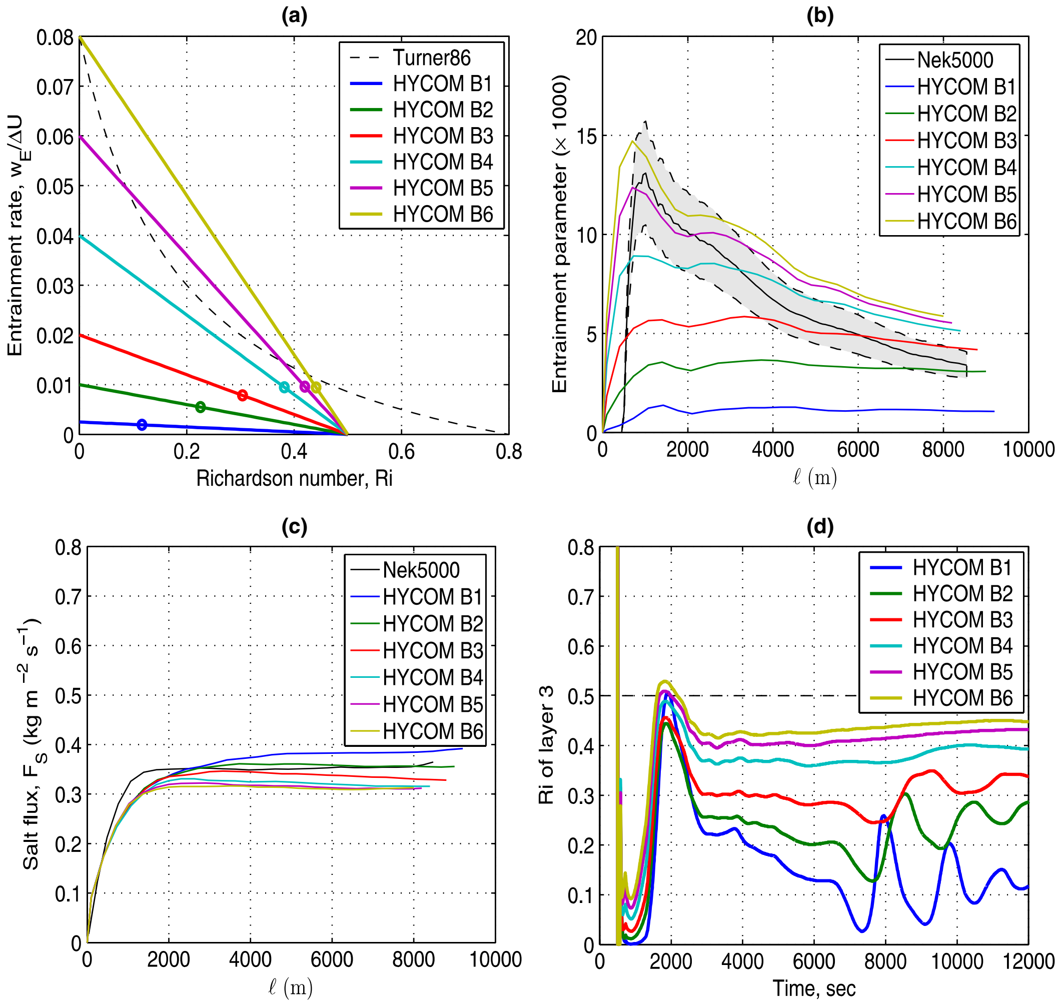

Fig. 6. The same as in Fig. 5 but for Exp. B, $Ri_c = 0.50$.

either different or somewhat similar evolution of entrainment parameter $\mathscr{E}(\ell)$, we thus seek to obtain the optimal values of E_0 and Ri_c in Eq. (16) or an envelope of functions from which a unified scheme could be developed.

Following this consideration, four experiment sets, A, B, C, and D, corresponding to four different values of Ri_c (Table 2), are performed. Each set is tested with six different values of E_0. The chosen range of $Ri_c = 0.25$ to $Ri_c = 0.75$ spans plausible values between the linear stability threshold of stratified shear flows (Miles, 1961) and the onset of turbulence in laboratory experiments (Rohr et al., 1988) to the cut-off bulk Richardson numbers (Turner, 1986). Intermediate values of $Ri_c = 0.50$ and $Ri_c = 0.35$ are included to increase the information content. The chosen values of E_0 are based on the experience acquired when comparing the HYCOM experiments to the Nek5000 simulations.

For each experiment, the entrainment parameter $\mathscr{E}(\ell)$ and the salt flux $F_S(\ell)$ are calculated from the HYCOM simulations and compared to the results from Nek5000 as described in Section 4.1. Considering the large number of parameter combinations, the comparison is conducted for $\theta = 1°$ only. An optimal parameterization function derived from these comparisons is then tested for all slopes of 1°, 2°, 3°, and 4° in Section 4.3.

4.2.1. Exp. A: $Ri_c = 0.75$

Fig. 5 summarizes the results of the experiment set A. The parameterization function with varying E_0 are plotted together with the original TP (i.e., Eq. (3)) for comparative purposes (Fig. 5a). The criterion for a good entrainment parameterization is that it should be able to capture the evolution of $\mathscr{E}$ along ℓ for different slope

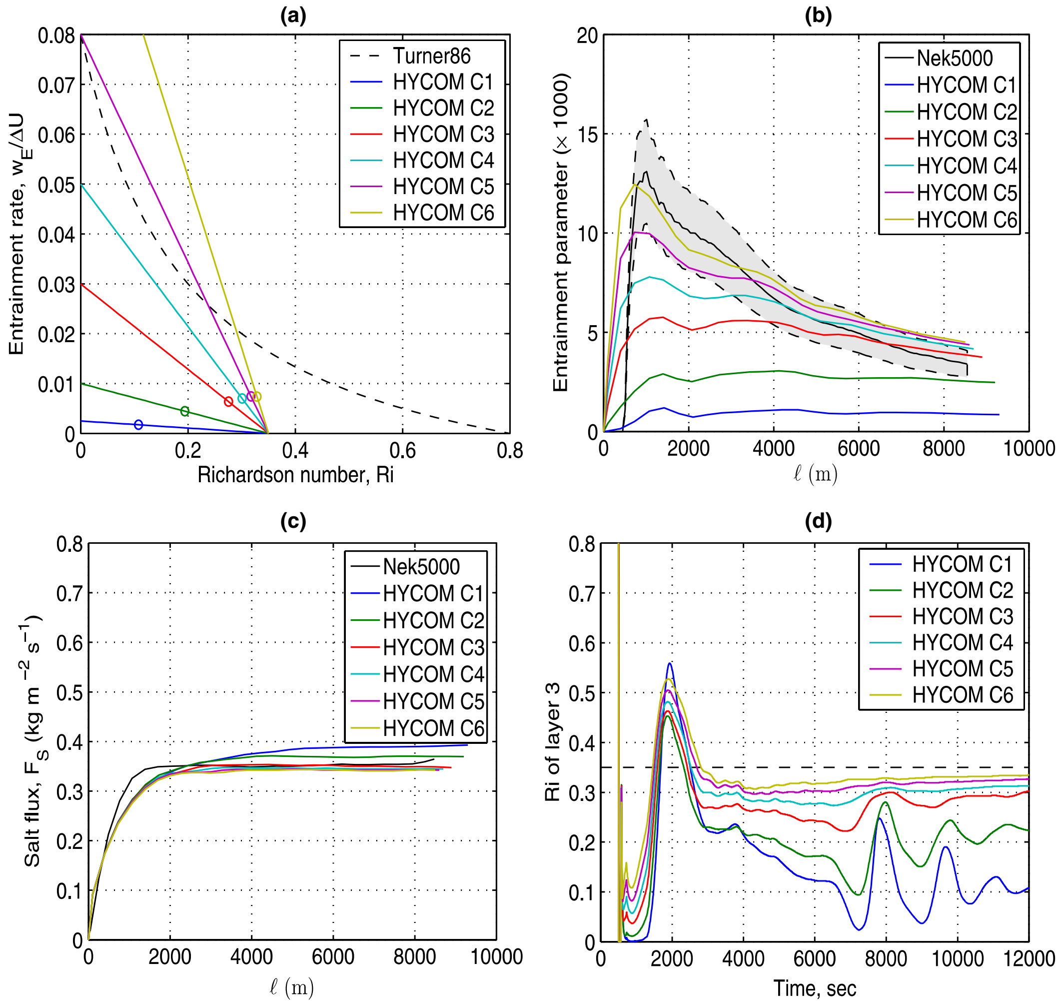

Fig. 7. The same as in Fig. 5 but for Exp. C, $Ri_c = 0.35$.

angles. In order to account for experimental design errors, we somewhat arbitrarily define that the result will be acceptable as long as they are within a ±20% tolerance band (Fig. 5b). Twenty percent is also the range of variability shown by Nek5000 when the slope is varied by 1° (Fig. 4a). The evolution of $\mathscr{E}(\ell)$ in Exp. A for the different values of E_0 differs in HYCOM when compared to the Nek5000. First, the entrainment occurs earlier in HYCOM. This is because it takes some time and distance for the plume in Nek5000 to develop turbulence (and entrainment), while such development process is not in HYCOM. Second, $\mathscr{E}(\ell)$ in Nek5000 reaches a maximum value of about 0.013 shortly after the plume passes X_0, and decays throughout the time thereafter. In HYCOM, it either attains an equilibrium state and does not decay (A1–A3) or does reach a maximum comparable to Nek5000 but then decays more slowly (A4–A6). Hence, none of these six parameterizations results in a satisfactory evolution of $\mathscr{E}(\ell)$.

In Exp. A, HYCOM and Nek5000 behave more similarly in terms of $F_S(\ell)$ than $\mathscr{E}(\ell)$, both showing small variations after the initial transients (Fig. 5c). This is not surprising since the boundary forcing largely determines the salt flux. The variation of F_S from run A1 to A6 suggests that a stronger entrainment leads to a slightly weaker salt flux.

Since the entrainment rate E is parameterized as a function of the Richardson number Ri, the actual value of Ri in the simulated gravity currents is an important diagnostic of the entrainment process. In HYCOM, the Richardson numbers are defined at the center of each layer (i.e., Eq. (5)). Fig. 5d plots the $Ri(t)$ of layer 3 at $x = X_0$ in HYCOM. Layer 3 is the upper-most layer within the plume and the location of the most vigorous

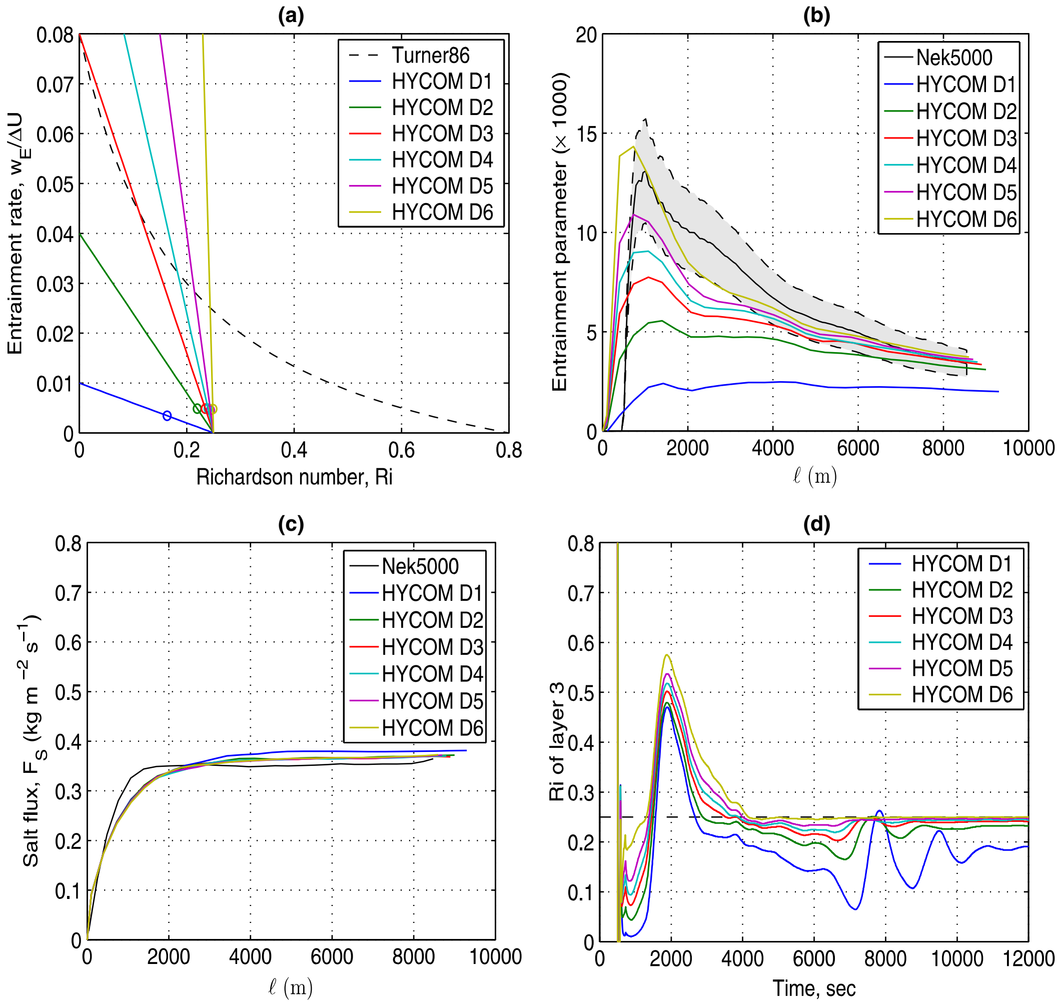

Fig. 8. The same as in Fig. 5 but for Exp. D, $Ri_c = 0.25$.

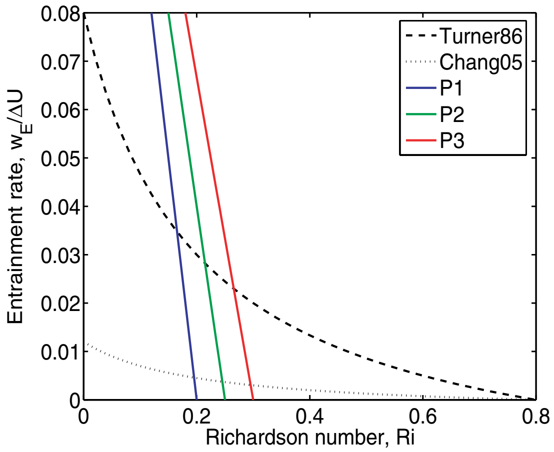

Fig. 9. Entrainment rate $E \equiv w_E/\Delta U$ as function of Richardson number Ri. The solid blue, green and red lines are linear function Eq. (16) with parameters $E_0 = 0.20$ and $Ri_c = 0.20$, 0.25, and 0.30; the dash and dot black lines are the original TP and parameterization function of (Chang et al., 2005) with $C_A = 0.15$, respectively. (For interpretation of the references in color in this figure legend, the reader is referred to the web version of this article.)

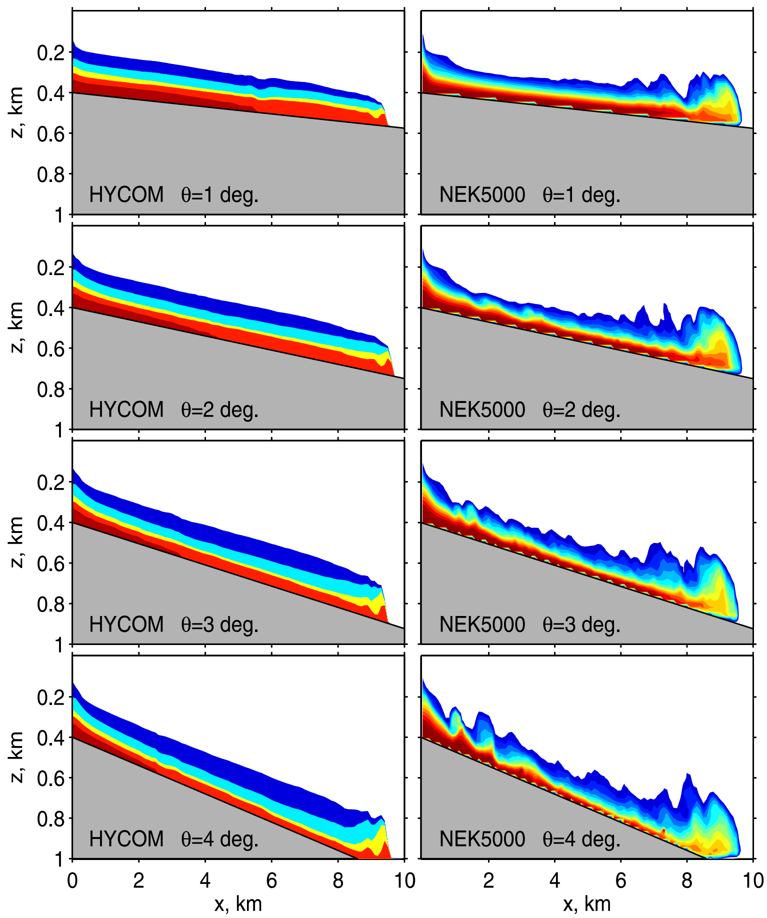

Fig. 10. Salinity snapshots when the gravity currents plume approaches the lower end of domain; HYCOM using P2 (left) and Nek5000 (right) with different bottom slopes (1–4°).

mixing. Ri is small when the head of plume passes X_0 and increases quickly due to the strong entrainment, then decreases and finally settles at some level ranging from 0.1 to 0.6, depending on the strength of the entrainment. Stronger entrainment results in larger Ri because the entrainment reduces the velocity shear and increases the plume thickness, two factors that tend to increase Ri. Changes in Ri in turn affect the entrainment through the inverse proportionality of E to Ri in (16). The time-averaged Ri ($t > 6000$ s) is marked by circles in Fig. 5a, which indicates that, for different E_0, different parts of $f(Ri)$ are active in determining the strength of entrainment $\mathscr{E}$. As a result, although an increase in E_0 simply results in a corresponding increase in $\mathscr{E}$, the increase in $\mathscr{E}$ becomes progressively smaller as E_0 becomes large. This tendency is more pronounced in experiment sets B, C, and D than in A.

4.2.2. Exp. B: $Ri_c = 0.50$

Results of experiment set B are depicted in Fig. 6 similarly to Fig. 5. The prescribed entrainment functions E of B1–B6 are shown with the original TP in Fig. 6a. As in Exp. A, none of these six experiments is able to capture the evolution of $\mathscr{E}$ along ℓ, although some improvement is shown in runs B5 and B6 (Fig. 6b). The F_S in the runs of Exp. B also show slight improvement over Exp. A (Fig. 6c). Stronger entrainment causes the Ri to be larger (Fig. 6d), and since E decreases faster with increasing Ri in Exp. B than in A, the feedback of Ri onto the entrainment becomes more significant.

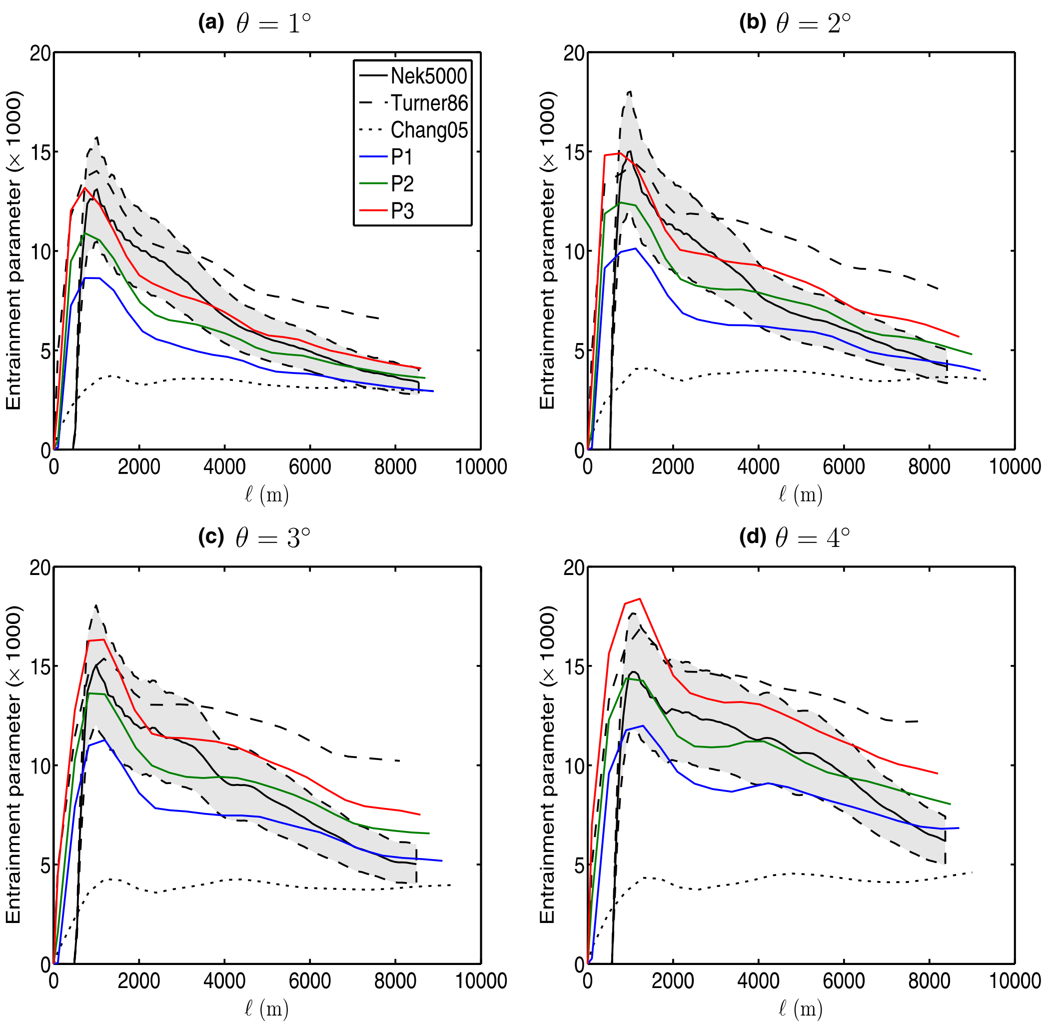

Fig. 11. Entrainment parameter $\mathscr{E}(\ell)$ from Nek5000 and HYCOM experiments with different bottom slopes. The Nek5000 results appears with shaded ±20% variance; five entrainment schemes in HYCOM are Turner (1986), Chang et al. (2005), P1, P2, and P3, respectively.

4.2.3. Exp. C: $Ri_c = 0.35$

We further reduce the Ri_c to 0.35 in experiment set C (Fig. 7). Even though E_0 spans a large range, $\mathscr{E}$ becomes close to the ±20% tolerance band later in time. Experiment C5 and C6 also show good matches in the entrainment maximum, thus improve the overall evolution of $\mathscr{E}(\ell)$. Corresponding to smaller variation in $\mathscr{E}$, the variations in F_S and Ri are also reduced. All six runs produce excellent matches in $F_S(\ell)$ to Nek5000. The narrow variability range of Ri can be explained by invoking the steady state momentum balance of gravity currents. The buoyancy forcing is balanced by bottom- and entrainment-stress. For the latter to be significant, Ri has to be in a range where $E(Ri)$ is large enough to allow for a momentum balance. Hence, upon the change of $E(Ri)$ to a steeper function with shorter range in Ri from Exp. A and B to C, the simulated Ri settles into a narrower range.

4.2.4. Exp. D: $Ri_c = 0.25$

Results of experiment D with $Ri_c = 0.25$ and E_0 of 0.01–1.0 are illustrated in Fig. 8. As expected following the trend from Exp. A to C, the variability ranges of $\mathscr{E}(\ell)$, $F_S(\ell)$ and $Ri(t)$ become even smaller. The $\mathscr{E}(\ell)$ of experiments D2–D6 closely follow the Nek5000 result after $\ell > 6000$ m (Fig. 8b). Meanwhile, runs D5 and D6 also reproduce an $\mathscr{E}$ maximum comparable to Nek5000, and thus match the time-dependent behavior of the corresponding Nek5000 runs better than the previous three sets. The $F_S(\ell)$ of the six runs in Exp. D are nearly

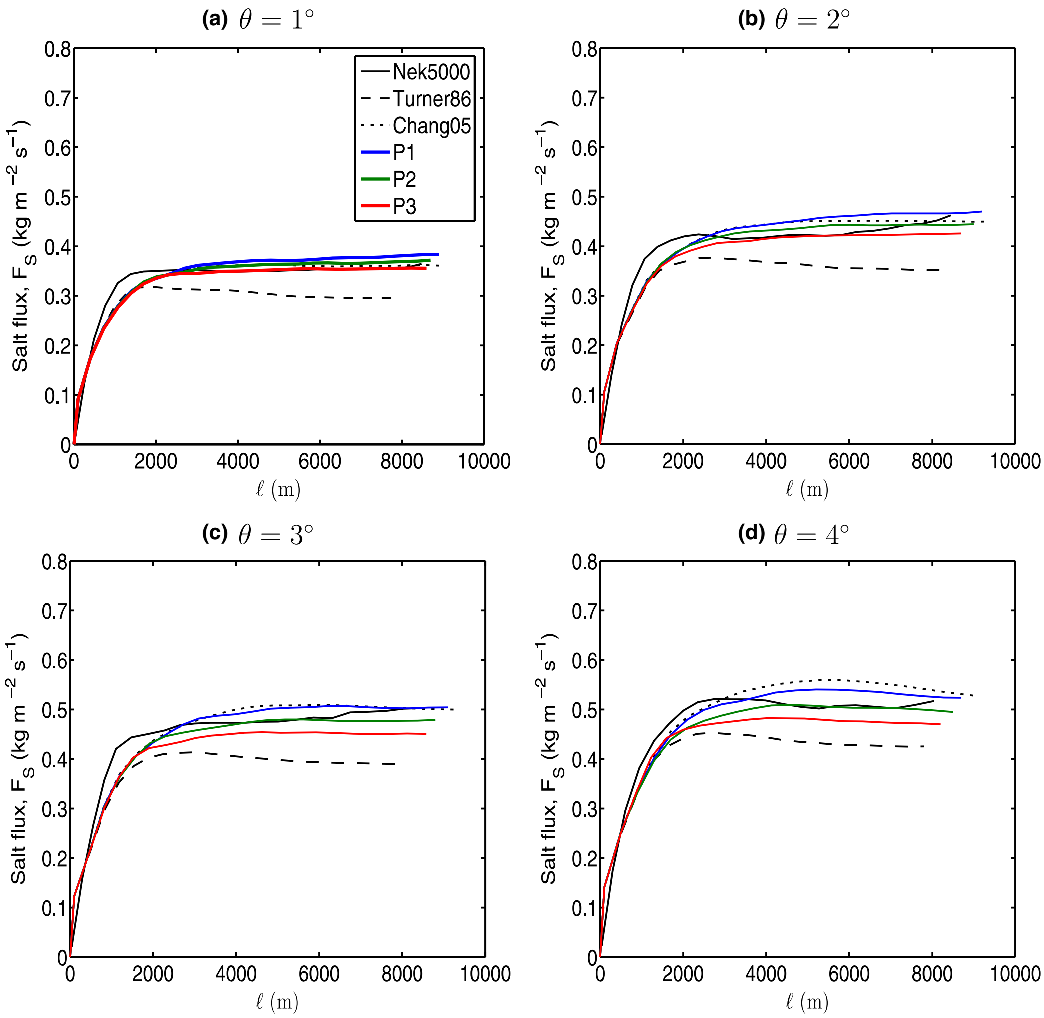

Fig. 12. Salt flux $F_S(\ell)$ from Nek5000 and HYCOM experiments with different bottom slopes.

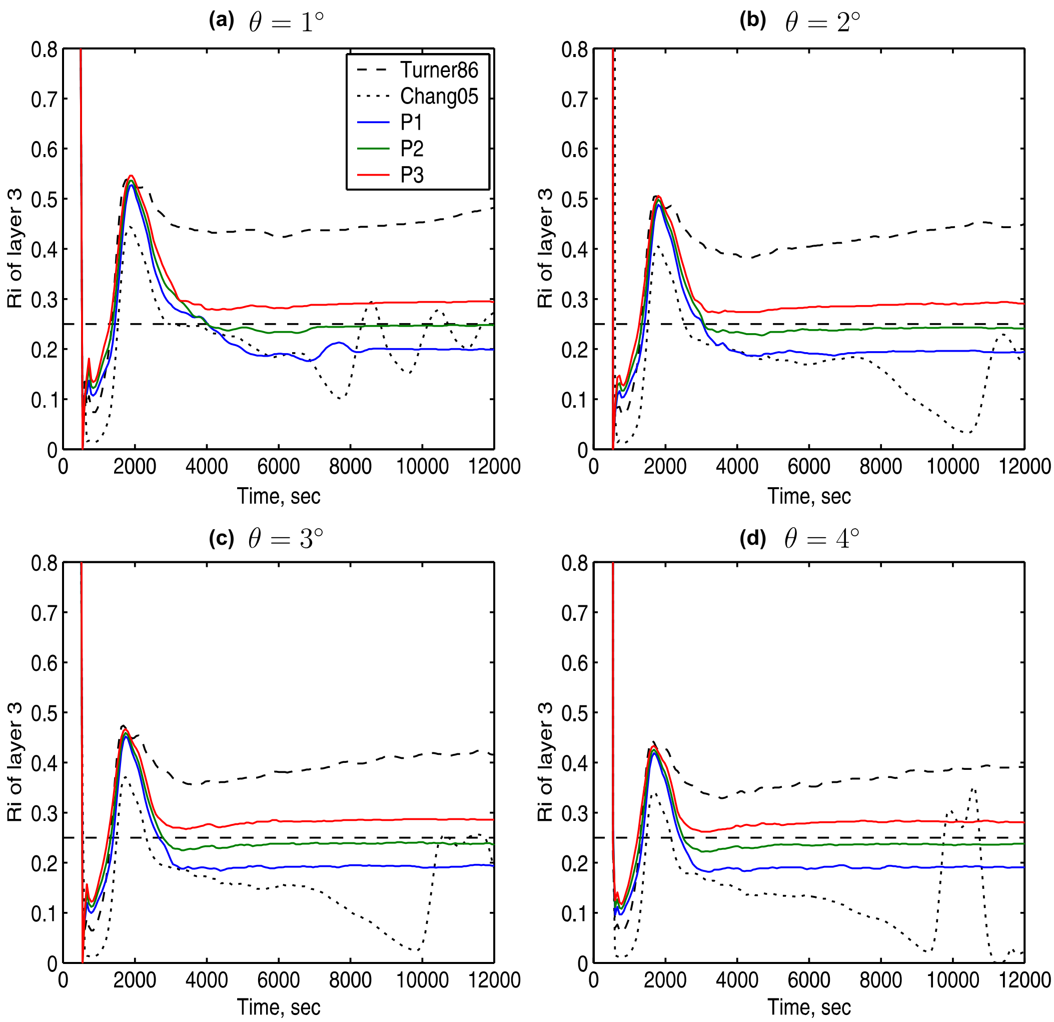

Fig. 13. Richardson numbers $Ri(t)$ of layer 3 at $x = X_0$ from HYCOM experiments with different bottom slopes. The dash line marks $Ri = 0.25$.

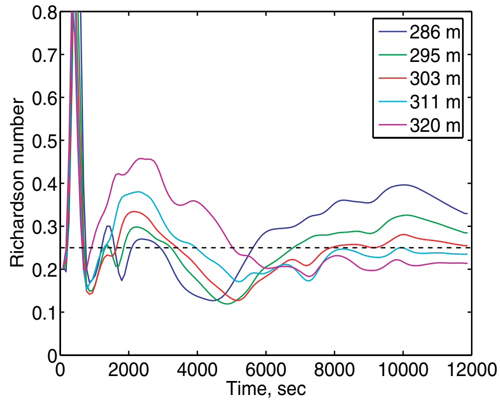

Fig. 14. Richardson numbers $Ri(t)$ at different depths at $x = X_0$ from Nek5000 experiment with $\theta = 1°$. The dash line marks $Ri = 0.25$.

identical, and the steep curve in $E(Ri)$ forces the flow into a narrow range $Ri(t) \approx Ri_c$ for the same reason as laid out above.

4.2.5. Optimal values of Ri_c and E_0 in linear parameterization $E = f(Ri)$

By experimenting with various combinations of the cut-off Richardson number Ri_c and the "amplitude" parameter E_0, we have found that the linear function $E = f(Ri)$ from experiments D5 and D6 produces the best match to the Nek5000 in terms of $\mathscr{E}$ as a function of ℓ. This simple parameterization states that there is no entrainment until Ri decreases below a critical value of about 0.25, and the entrainment increases linearly with decreasing Ri. $Ri_c \approx 0.25$ is consistent with our physical understanding of mixing in that the turbulence in stratified shear flows is suppressed for $Ri > 1/4$ and grows for $Ri < 1/4$ (e.g., Miles, 1961; Rohr et al., 1988).

A physical upper-limit for entrainment is $E_0 = 1.0$, which means that the maximum entrainment velocity w_E becomes the velocity difference ΔU itself. From experiment set D, we also observe that the evolution of $\mathscr{E}(\ell)$ is insensitive to E_0 as long as it is relatively large. This is because when mixing takes place, the strength of the mixing such that keeps the Ri close to its critical value. Hence, we set $E_0 = 0.20$ and $Ri_c = 0.25$ as the optimal

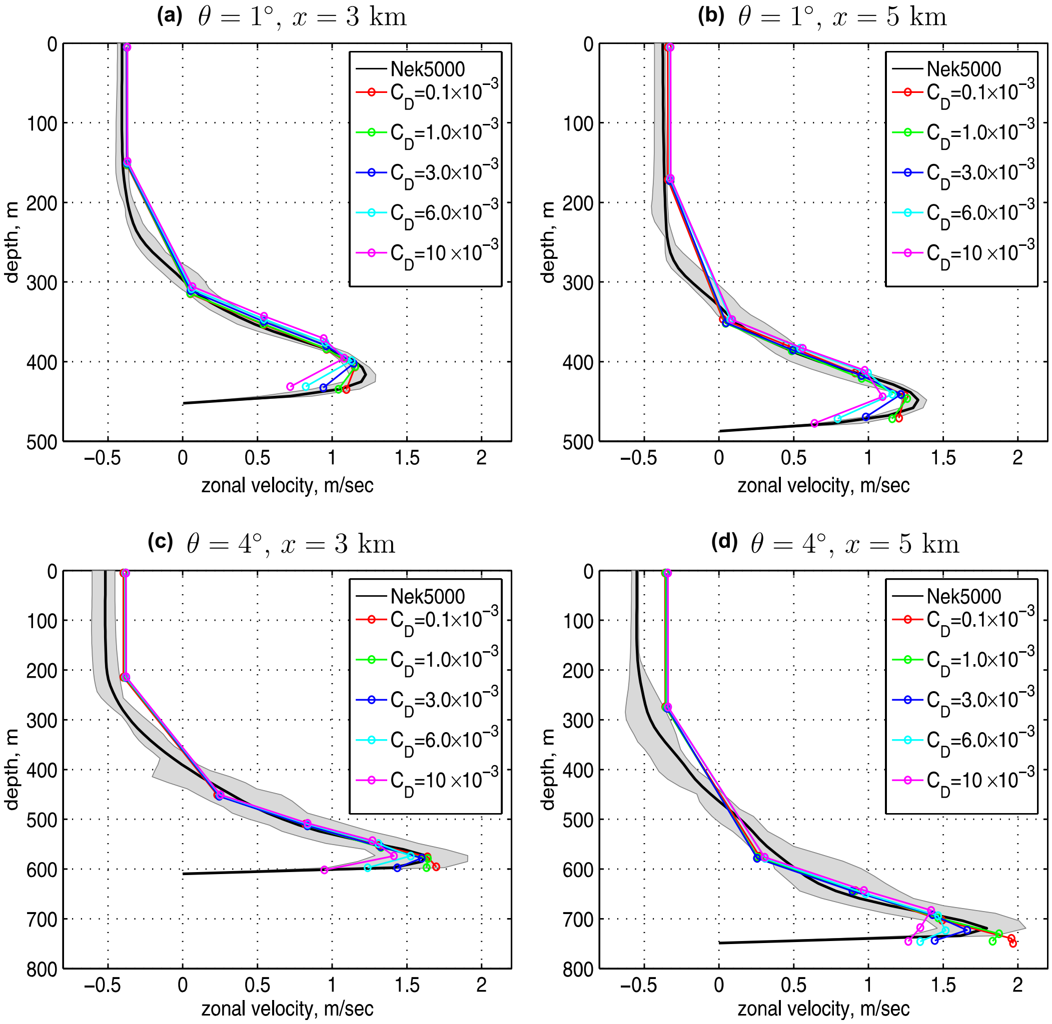

Fig. 15. Zonal velocity profiles at station $x = 3$ km (left panels) and $x = 5$ km (right panels) from Nek5000 and HYCOM with linear entrainment scheme P2. The black line is the mean profile from Nek5000 with shading area representing the time variation; five different C_Ds are tested in HYCOM, with center of each layer marked as "○". The upper and lower panels are 1° and 4° slope configuration, respectively.

values for entrainment parameterization (16). A variation of ±0.05 is applied to $Ri_c = 0.25$ to investigate the sensitivity of entrainment to the specific values of Ri_c. We simply call these parameterizations P1, P2, and P3 hereafter, for $E_0 = 0.20$ and $Ri_c = 0.20$, 0.25, and 0.30, respectively (Fig. 9).

4.3. Detailed comparison between HYCOM with optimal $f(Ri)$ and Nek5000

The next stage is to investigate whether our optimal parameterization produces reasonable results in response to varying slopes. Thus, we conduct the comparison for all four slope angles: $\theta = 1°$, 2°, 3°, and 4°. Before going into quantitative details, we first present a visual comparison between Nek5000 and HYCOM with entrainment scheme P2. Fig. 10 shows salinity anomaly snapshots of the simulated gravity currents approaching the lower end of the model domain in Nek5000 ($x = 10$ km). In Nek5000, fine-scale turbulent structures become more pronounced with increasing θ. This is not the case in HYCOM with P2 because none of the turbulence is resolved. For the same reason, the gravity current in Nek5000 has more pronounced head, a nonhydrostatic feature that is not entirely reproduced in HYCOM. While there are naturally some differences between the Nek5000 and HYCOM results, our simple parameterization appears to allow fairly realistic gravity current simulations with the latter.

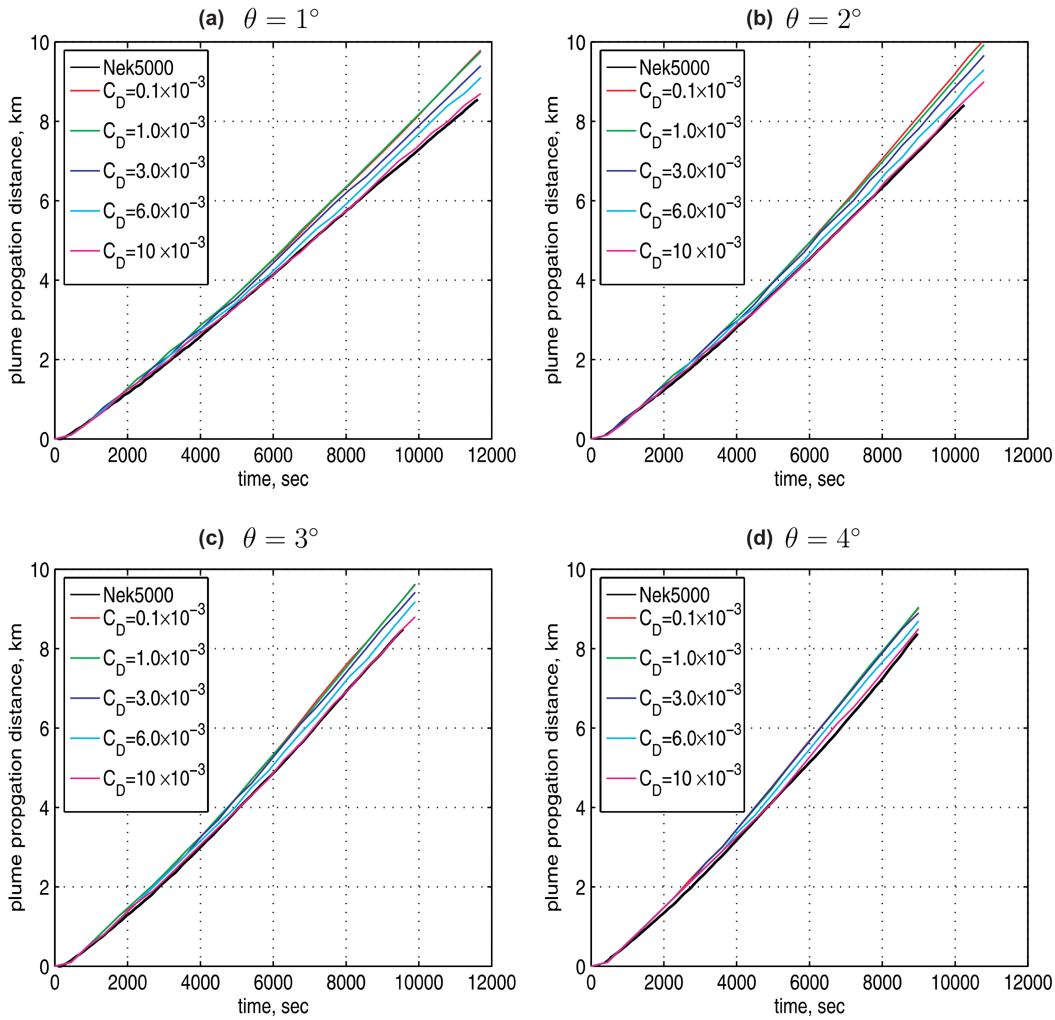

Fig. 16. The plume propagation distance ℓ vs. time from Nek5000 and HYCOM experiments with different bottom slopes. HYCOM is run with the linear entrainment scheme P2 and five bottom drag coefficients C_D.

4.3.1. Entrainment parameter $\mathscr{E}(\ell)$

Fig. 11 depicts $\mathscr{E}(\ell)$ from Nek5000 and HYCOM simulations for slope angle θ of 1–4°. The five curves in HYCOM are corresponding to the following entrainment schemes: TP by Hallberg (2000), Chang et al. (2005), P1, P2, and P3 (see Fig. 9), respectively. The original TP actually produces the high entrainment maximum quite well, but overestimates the entrainment rate as the plume develops further in time (similar to A5). Multiplication of the right hand side of Eq. (3) by a factor of 0.15 as in Chang et al. (2005) leads to an entrainment that is flat along ℓ with no decay. This behavior is similar to A2. Our optimal formula shows a satisfactory match in $\mathscr{E}(\ell)$ to Nek5000 for all four configurations. Fig. 11 also suggests that the $\mathscr{E}(\ell)$ is sensitive to the change in Ri_c.

4.3.2. Salt flux $F_S(\ell)$ and Richardson number $Ri(t)$

The salt flux F_S from HYCOM using P1, P2, and P3 compares well with that from Nek5000 (Fig. 12). The excess entrainment stress of the original TP slows down the plume and decreases the F_S for all four slope angles, while the lack of entrainment in Chang et al. (2005) leads to slightly larger F_S especially for large θ.

For configurations with increasing θ, the $Ri(t)$ show very similar evolution pattern, but decrease slightly (Fig. 13). This partially contributes to the increase in entrainment as seen in Fig. 11. As expected, the $Ri(t)$ of P1, P2, and P3 finally settle at levels close to the corresponding Ri_c of 0.20, 0.25, and 0.30. In contrast, the original TP and Chang et al. (2005) operate over a larger range of Ri. Therefore, the time evolution of Ri at the interface between the gravity current and ambient water appears to be a characteristic feature of different parameterizations. Based on the spanwise-averaged velocity and salinity anomaly profiles taken at $x = X_0$, we calculated $Ri(t)$ from Nek5000 in experiment with $\theta = 1°$ (Fig. 14). The five selected depths are within the high shear interface where the most intense mixing takes place. These $Ri(t)$s are thus comparable those of layer 3 in HYCOM (Fig. 13a). The comparison shows that $Ri(t)$ in Nek5000 and in HYCOM with entrainment scheme P2 are in reasonable agreement in terms of both magnitude and time evolution, providing further support for the parameterization.

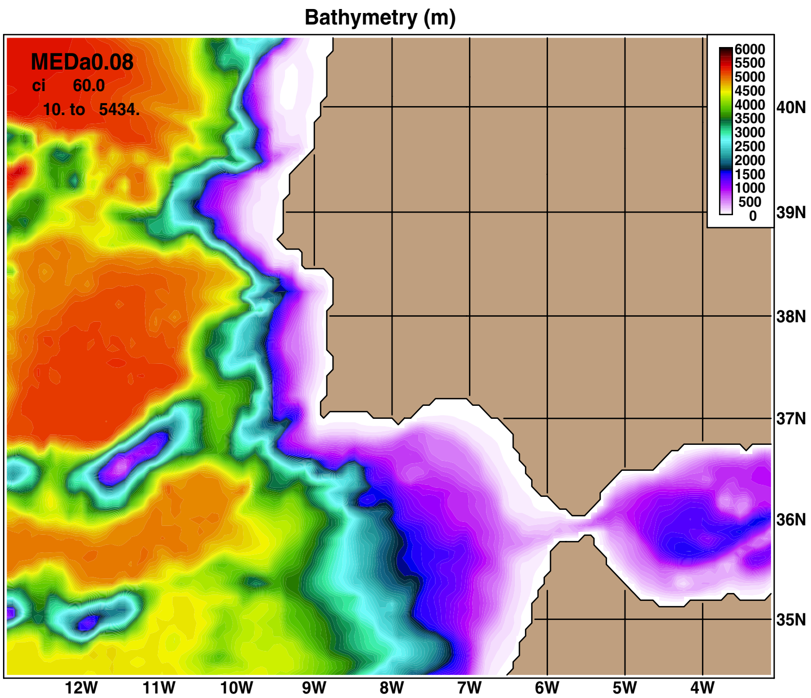

Fig. 17. Model topography of the eastern North Atlantic Ocean, the Gulf of Cadiz and western end of the Mediterranean Sea.

4.3.3. Velocity profile U(z) and plume propagation speed

In addition to the fundamental differences in model formulation, Nek5000 and HYCOM differ in treating the bottom stress. Due to a high spatial resolution, the bottom boundary layer is naturally resolved in Nek5000. In HYCOM an empirical quadratic drag law is applied in the lowest 10 m with a constant drag coefficient C_D. In a sensitivity test in HYCOM with P2, C_D is varied by two orders of magnitude (from 0.1×10^{-3} to 10×10^{-3}). Fig. 15 shows two time-averaged vertical profiles of zonal velocity at $x = 3$ and 5 km in experiments with $\theta = 1°$ and 4°. The comparison suggests that, except for $C_D = 0.1 \times 10^{-3}$, HYCOM with the quadratic drag scheme works fairly well in reproducing the velocity profiles from Nek5000, and the results are sensitive to C_D only near the very bottom. Our primary concern is to have a comparable propagation speed of the plume since ℓ directly affects the calculation of $\mathscr{E}$ and F_S. Fig. 16 suggests that for all four configurations, $C_D = 10 \times 10^{-3}$ shows the best match in $\ell(t)$ to the Nek5000 and this value has therefore been chosen for all the experiments discussed previously. The plume propagation speed is however not very sensitive to the value of C_D. With two orders of variation in C_D, $\ell(t)$ changes only about 10% for $\theta = 1°$, even less for $\theta > 2°$.

In summary, with a simple optimal parameterization, HYCOM is shown to reproduce qualitatively the salinity anomaly distribution, and quantitatively the evolutions of entrainment $\mathscr{E}(\ell)$ (Fig. 11), salt flux $F_S(\ell)$ (Fig. 12), Richardson number $Ri(t)$ (Fig. 14), velocity profile (Fig. 15) and propagation speed (Fig. 16) of the bottom gravity current flow down different slope angles as in Nek5000.

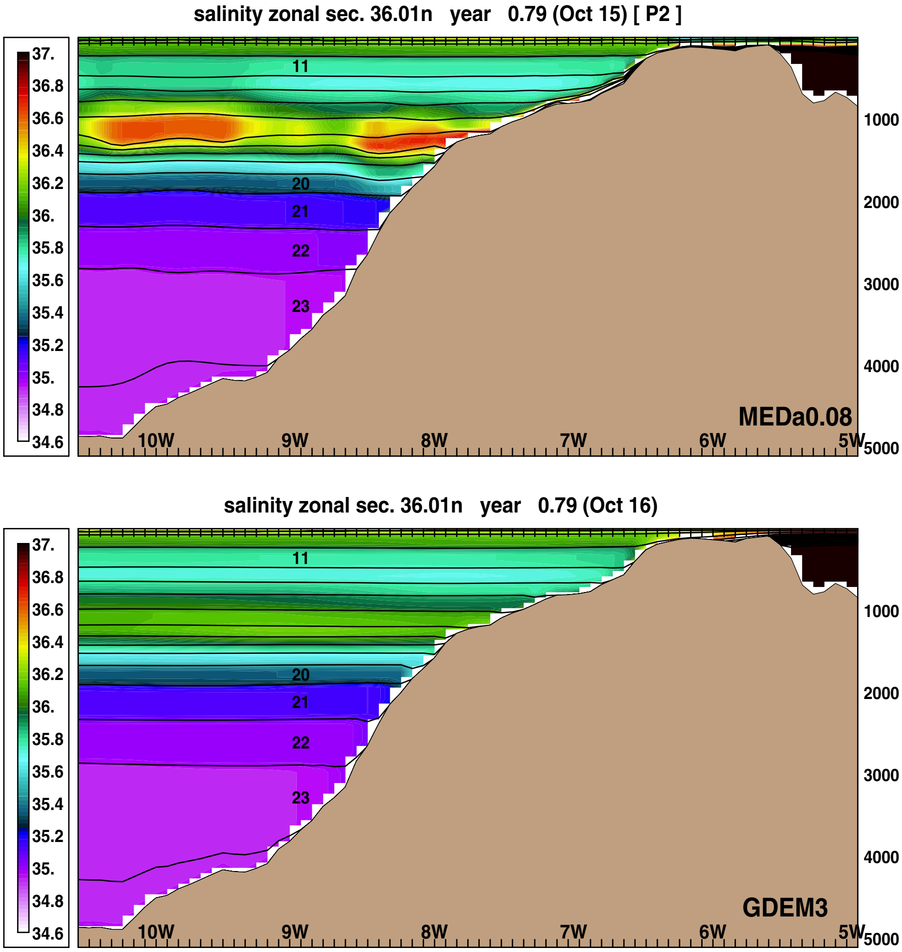

Fig. 18. Salinity distribution at a zonal section near 36°N from HYCOM simulation (upper panel) with entrainment scheme P2 and the GDEM3 climatological data (lower panel).

5. Realistic simulation of the Mediterranean overflow

We now evaluate the performance of the optimal parameterization in realistic oceanic overflow scenarios. Several reasons lead us to choose the Mediterranean outflow as our test bed. It is important for the water-mass formation of mid-depth subtropical North Atlantic Ocean, and it is one of the best-observed outflows (e.g., Ambar and Howe, 1979; Ochoa and Bray, 1991; Wesson and Gregg, 1994; Johnson et al., 1994a,b; Baringer and Price, 1997a,b etc.). The source water of Mediterranean outflow is so saline and dense—$\theta = 13$ °C, $S = 38.45$ psu, and $\sigma_\theta = 28.95\ \mathrm{kg\ m^{-3}}$—that it would sink to the bottom of the North Atlantic Ocean in the absence of mixing. This is what happens in isopycnic coordinate models when the diapycnal mixing is turned off. On the other hand, excess entrainment of North Atlantic Central Water into the outflow could result in a shallower equilibrium depth. Thus, the equilibration depth and properties of the product water masses can serve as simple and effective measures for the fidelity of the entrainment parameterizations.

The model configuration is similar to that of Papadakis et al. (2003), who used the same model as herein along with a variant of the TP scheme (3). In that study, the basic features of the Mediterranean outflow were reproduced, and the outflow water mass equilibrated at a reasonable depth. But further applications with different configurations led to too shallow Mediterranean outflows, in agreement with the recent study of Chang et al. (2005). The horizontal resolution used is 1/12° (~7 km), and there are 28 σ_2 layers in the vertical. There is no surface forcing, and all boundaries are closed. The model is integrated for 6 months. Apart from the

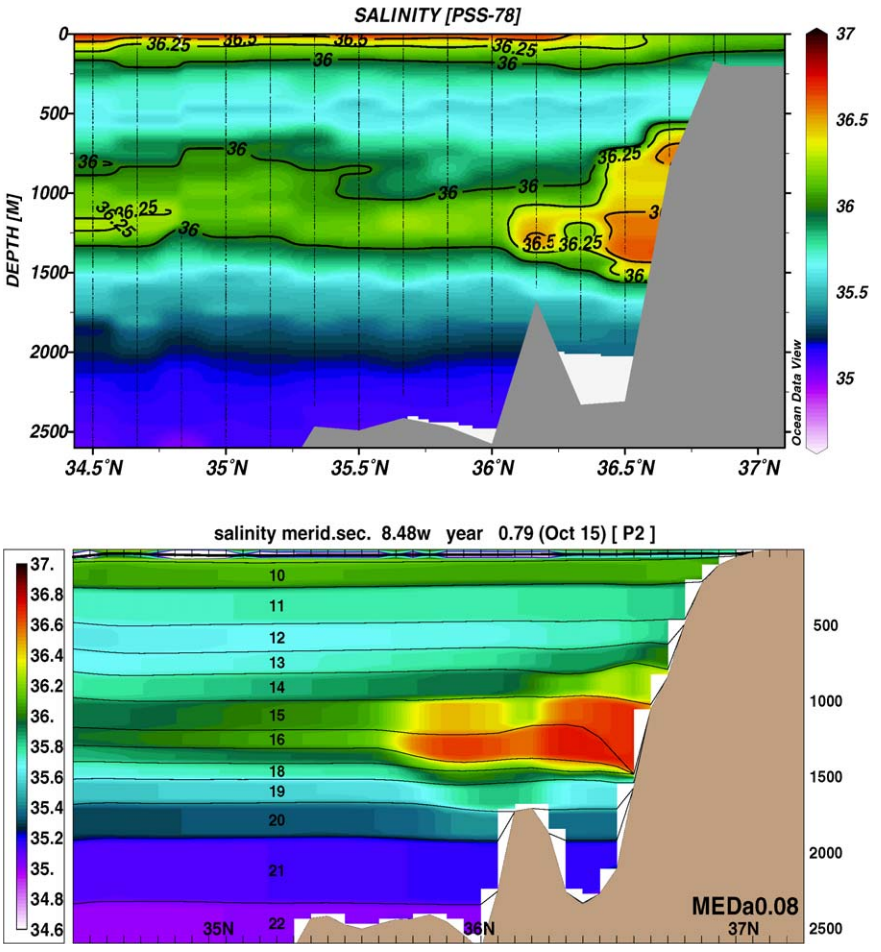

Fig. 19. Salinity distributions at meridional section near 8.5°W: (upper panel) CTD data from WOCE cruises AR16 and AR06; (lower panel) HYCOM simulation with entrainment scheme P2.

entrainment parameterization and layer set-ups, the primary difference of our present model configuration from that of Papadakis et al. (2003) is that we include a small part of western Mediterranean Sea in which T and S are relaxed to climatology in order to provide the outflow source water. This eliminates the need to specify inflow/outflow velocity, temperature and salinity profiles at western end of the Strait of Gibraltar. The bathymetry of the model domain is shown in Fig. 17. Three simulations are performed that differ only by entrainment parameterization: (a) our optimal entrainment scheme P2, (b) KPP (Eq. (1)), and (c) TP (Eq. (3)).

Fig. 18 shows the simulated salinity field with P2 at a zonal section near 36°N as well as the corresponding section from climatological data GDEM3 (General Digital Environmental Model). After flowing out of the Strait of Gibraltar, the simulated Mediterranean water begins to descend along the continental slope where it mixes with overlying water. It finally achieves neutral buoyancy at layers 15, 16, and 17, corresponding to $\sigma_2 = 36.52$, 36.62, and 36.70 kg m^{-3}, respectively. While the depth of the high salinity tongue agrees between model and GDEM3, the maximum salinity is considerably higher in HYCOM than in the smoothed climatology. We thus conduct a further comparison with a directly observed CTD data from WOCE cruise AR16 and AR06 (September 2–12, 1991) at ~8.5°W (Schlitzer, 2003). The simulation with P2 shows agreement with the observation both in terms of the neutral buoyancy level and the salinity of the product water mass (Fig. 19). In contrast, the simulated outflow water mass equilibrates deeper than observed with KPP and shallower with TP (Fig. 20), which indicates that the entrainment is under-prescribed in Eq. (1) and over-prescribed in Eq. (3).

As a final illustration, Fig. 21 presents a plan view of salinity and horizontal velocity fields of layer 15 in the Gulf of Cadiz. The outflow water follows the northern slope of the Gulf until the Cape of Saint Vincent. Two eddy structures can be identified. One located at west of the Cape of Saint Vincent, which is a major formation site of Mediterranean eddies (Bower et al., 2002), and the other is in the Gulf near 8° W, where dipole struc-

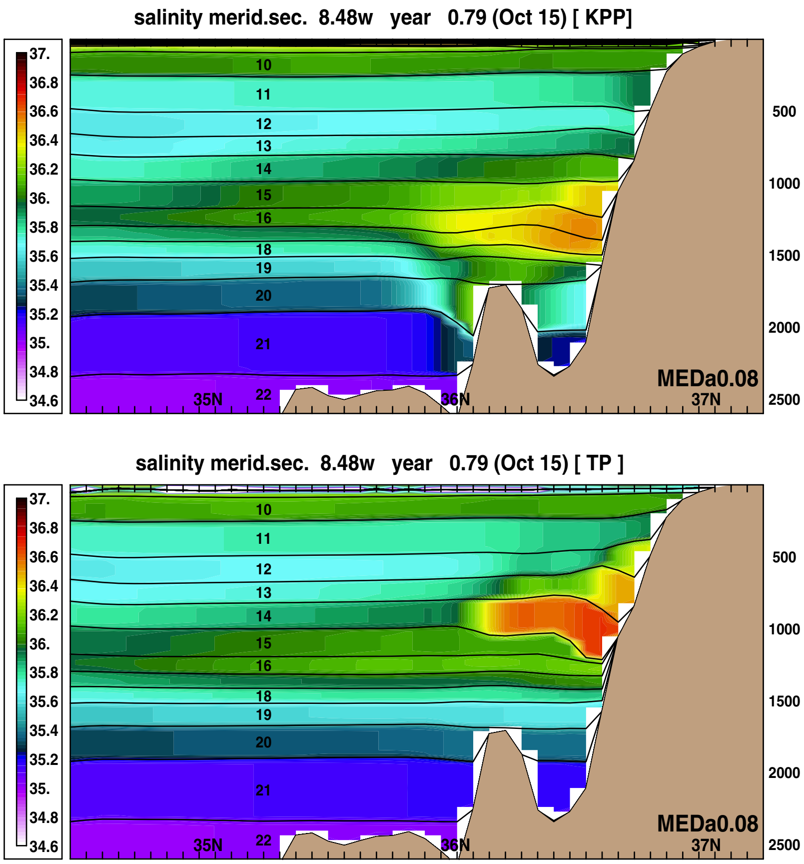

Fig. 20. Simulated salinity distributions at meridional section near 8.5°W with the KPP (upper panel) and the original TP (lower panel).

tures have been observed with subsurface floats (Serra and Ambar, 2002). A detailed discussion of the outflow water beyond the Gulf of Cadiz is outside the scope of this paper.

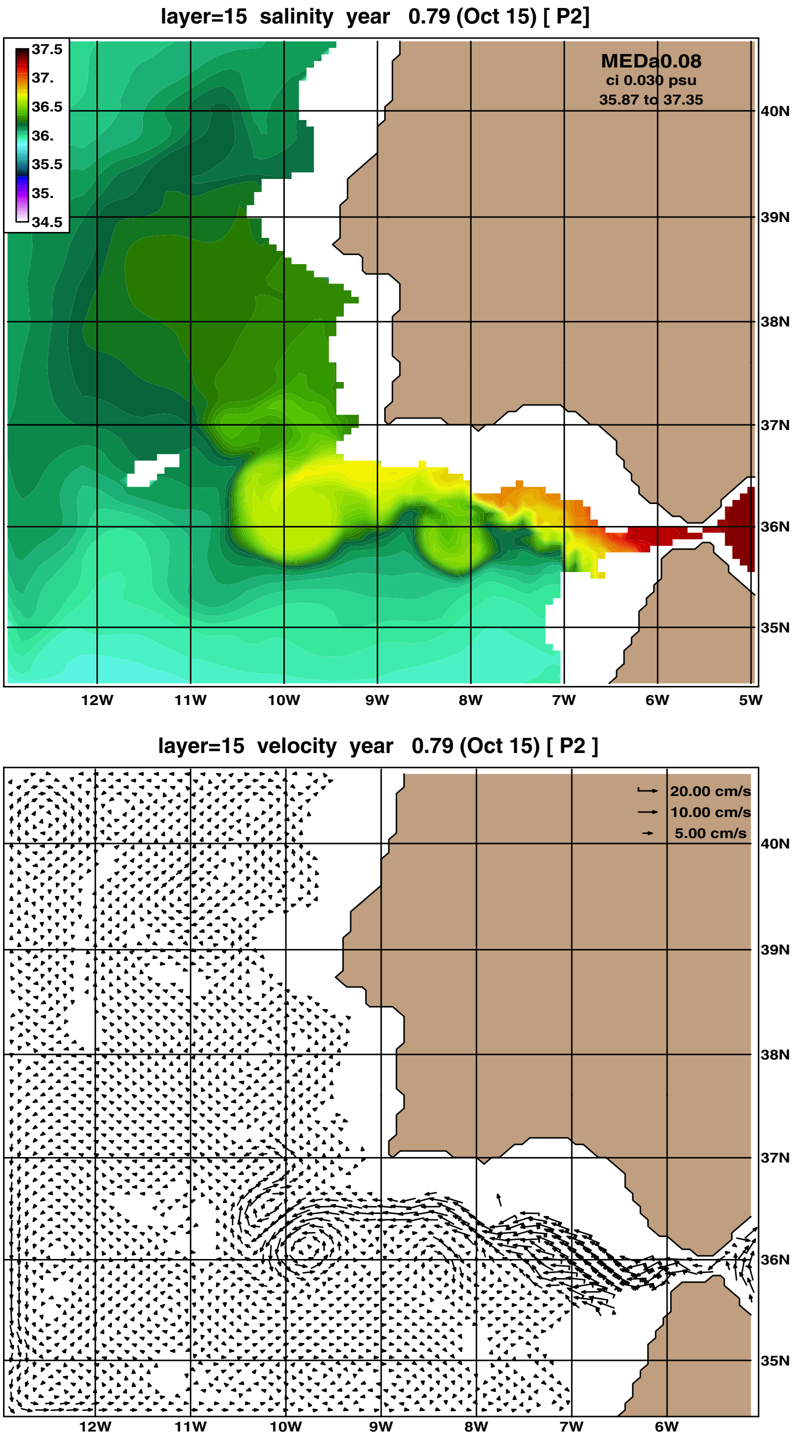

Fig. 21. Horizontal distribution of the salinity and velocity fields in layer 15 from HYCOM simulation using entrainment scheme P2.

6. Summary and discussion

In light of the pressing need for reliable and physically based parameterizations of mixing of overflows with ambient water masses in OGCMs, a new algebraic parameterization for isopycnic coordinate models is derived based on the work by Turner (1986) and Hallberg (2000). The parameterization casts the entrainment velocity as a function of the Richardson number (Ri) times the velocity difference across layers, incorporating a dependence on the forcing. This formulation is consistent with the Buckingham's Pi-Theorem (e.g., Kundu, 1990) which states that constants in a physical law should be dimensionless and with the physical requirement that the interfacial shear is the dominant energy source for turbulent mixing in stratified flows.

To determine the function $f(Ri)$, we compare the simulated gravity currents flowing down various bottom slopes from the relatively low-resolution, hydrostatic model HYCOM to that from the high-resolution, non-hydrostatic spectral element model Nek5000, which serves as ground truth. A linear function, $E = E_0(1 - Ri/Ri_c)$, in which E_0 and Ri_c represent the entrainment magnitude and the cut-off Richardson number, is used in HYCOM with a 1° slope and the results are quantified by an entrainment parameter $\mathscr{E}(\ell)$ and a salt flux $F_S(\ell)$. The comparison shows that $\mathscr{E}(\ell)$ is quite sensitive to the variations in E_0 and Ri_c and that the best results were obtained for $E_0 = 0.20$ and $Ri_c = 0.25$. On the other hand, $F_S(\ell)$ is not very sensitive to the change in E_0 and Ri_c, and compares well to the Nek5000 in all simulations.

This simple, optimal, linear scheme is then applied in four configurations varying in the bottom slope angle (1–4°). A detailed comparison of $\mathscr{E}(\ell)$, $F_S(\ell)$, $Ri(t)$, velocity profiles and propagation speeds is performed. The results suggest that HYCOM is able to reproduce the basic characteristics of the simulated gravity current from Nek5000 in qualitative and quantitative respects. In order to explore the performance of this scheme in realistic overflow applications, a simulation of the Mediterranean with realistic topography and water masses is carried out in a final test using HYCOM with horizontal resolution of 1/12°. The entrainment parameterization leads to a realistic equilibration depth of the outflow plume in the Gulf of Cadiz.

OGCMs used for climate studies require simple, yet physically based parameterizations of mixing in general and especially of the entrainment into gravity currents. The parameterization proposed herein, though radically simple, is consistent with the fundamental theoretical and laboratory results from stably stratified shear flows: the shear-induced turbulence grows (decays) in the regime of $Ri < 0.25$ ($Ri > 0.25$), respectively. It thus appears to hold promise for realism and deserves a more detailed evaluation by comparing the model results with observations in various overflow cases. A remaining issue that needs to be addressed is the dependence of the performance of the entrainment parameterization on the horizontal grid spacing. In the near future, this question will be investigated by carrying out a detailed comparison of model results with the observations of Baringer and Price (1997a,b) from the Mediterranean outflow.

Acknowledgements

We greatly appreciate the support of National Science Foundation via grants OCE 0336799 and OCE 0352047 and of the National Ocean Partnership Program (NOPP) via award N000140410676. The authors benefited greatly from discussions with the other PIs of the Climate Process Team on gravity current entrainment, G. Danabasoglu, T. Ezer, A. Gordon, S. Griffies, P. Gent, R. Hallberg, W. Large, S. Legg, J. Price, P. Schopf and J. Yang. We thank the two anonymous reviewers for their constructive criticism, which greatly improved the manuscript.

References

Ambar, I., Howe, M.R., 1979. Observations of the Mediterranean outflow. II. The deep circulation in the vicinity of the Gulf of Cadiz. Deep Sea Res. 26A, 555–568.

Baringer, M.O., Price, J.F., 1997a. Mixing and spreading of the Mediterranean outflow. J. Phys. Oceanogr. 27, 1654–1677.

Baringer, M.O., Price, J.F., 1997b. Momentum and energy balance of the Mediterranean outflow. J. Phys. Oceanogr. 27, 1678–1692.

Beckmann, A., Döscher, R., 1997. A method for improved representation of dense water spreading over topography in geopotential-coordinate models. J. Phys. Oceanogr. 27, 581–591.

Bleck, R., 2002. An oceanic general circulation model framed in hybrid isopycnic-Cartesian coordinates. Ocean Model. 37, 55–88.

Bower, A., Serra, N., Ambar, I., 2002. Structure of the Mediterranean undercurrent and Mediterranean water spreading around the southwestern Iberian Peninsula. J. Geophys. Res. 107 (C10), 3161. doi:10.1029/2001JC001007.

Britter, R.E., Linden, P.F., 1980. The motion of the front of a gravity current traveling down an incline. J. Fluid Mech. 99, 531–543.

Chang, Y., Xu, X., Özgökmen, T.M., Chassignet, E.P., Peters, H., Fischer, P.F., 2005. Comparison of gravity current mixing parameterizations and calibration using a high-resolution 3D nonhydrostatic spectral element model. Ocean Model. 10, 342–368.

Chassignet, E.P., Smith, L.T., Halliwell, G.R., Bleck, R., 2003. North Atlantic simulations with the hybrid coordinate ocean model (HYCOM): impact of the vertical coordinate choice, reference density, and thermobaricity. J. Phys. Oceanogr. 34, 2504–2526.

Ellison, T.H., Turner, J.S., 1959. Turbulent entrainment in stratified flows. J. Fluid Mech. 6, 423–448.

Ezer, T., Mellor, G., 2004. A generalized coordinate ocean model and comparison of the bottom boundary layer dynamics in terrain-following and in z-level grids. Ocean Model. 6, 379–403.

Fernando, H.J.S., 1991. Turbulent mixing in stratified fluids. Annu. Rev. Fluid Mech. 23, 455–493.

Fischer, P.F., 1997. An overlapping Schwarz method for spectral element solution of the incompressible Navier–Stokes equations. J. Comp. Phys. 133, 84–101.

Fischer, P.F., Mullen, J.S., 2001. Filter-based stabilization of spectral element methods. Comptes rendus de l'Académie des sciences Paris, t. 332, -Série I - Analyse numérique, pp. 265–270.

Fischer, P.F., Miller, N.I., Tufo, H.M., 2000. An overlapping Schwarz method for spectral element simulation of three-dimensional incompressible flows. In: Björstad, P., Luskin, M. (Eds.), Parallel Solution of Partial Differential Equations. Springer-Verlag, pp. 159–181.

Girton, J.B., Sanford, T.B., 2003. Descent and modification of the overflow plume in the Denmark Strait. J. Phys. Oceanogr. 33, 1351–1363.

Girton, J.B., Sanford, T.B., Käse, R.H., 2001. Synoptic sections of the Denmark Strait overflow. Geophys. Res. Lett. 28, 1619–1622.

Gordon, A., Zambianchi, E., Orsi, A., Visbeck, M., Giulivi, C., Whitworth III, T., Spezie, G., 2004. Energetic plumes over the western Ross Sea continental slope. Geophys. Res. Lett. 31, L21302. doi:10.1029/2004GL020785.

Griffies, S.M., Pacanowski, R.C., Hallberg, R.W., 2000. Spurious diapycnal mixing associated with advection in a *z*-coordinate ocean model. Mon. Weather Rev. 128, 538–564.

Hallberg, R., 2000. Time integration of diapycnal diffusion and Richardson number dependent mixing in isopycnal coordinate ocean models. Mon. Weather Rev. 128, 1402–1419.

Halliwell, G.R., 2004. Evaluation of vertical coordinate and vertical mixing algorithms in the hybrid-coordinate ocean model (HYCOM). Ocean Model. 7, 285–322.

Johnson, G.C., Sanford, T.B., Baringer, M.O., 1994a. Stress on the Mediterranean outflow plume: Part I. Velocity and water property measurements. J. Phys. Oceanogr. 24, 2072–2083.

Johnson, G.C., Lueck, R., Sanford, T.B., 1994b. Stress on the Mediterranean outflow plume: Part II. Turbulent dissipation and shear measurements. J. Phys. Oceanogr. 24, 2084–2092.

Jungclaus, J.H., Mellor, G., 2000. A three-dimensional model study of the Mediterranean outflow. J. Mar. Syst. 24, 41–66.

Keulegan, G.H., 1958. The motion of saline fronts in still water. Tech. Rep. 5831, U.S. Nat. Bur. Stand.

Killworth, P.D., Edwards, N.R., 1999. A turbulent bottom boundary layer code for use in numerical ocean models. J. Phys. Oceanogr. 29, 1221–1238.

Kundu, P.K., 1990. Fluid Mechanics. Academic Press, Inc, San Diego, CA.

Large, W.G., 1998. Modeling and parameterizing ocean planetary boundary layer. In: Chassignet, E., Verron, J. (Eds.), Ocean Modelling and Parameterization. Kluwer, pp. 45–80.

Large, W.G., Gent, P.R., 1999. Validation of vertical mixing in an equatorial ocean model using large eddy simulations and observations. J. Phys. Oceanogr. 29, 449–464.

Large, W.G., McWilliams, J.C., Doney, S.C., 1994. Ocean vertical mixing: a review and a model with a nonlocal boundary layer parameterization. Rev. Geophys. 32, 363–403.

Large, W.G., Danabasoglu, G., Doney, S.C., McWilliams, J.C., 1997. Sensitivity to surface forcing and boundary layer mixing in a global ocean model: annual-mean climatology. J. Phys. Oceanogr. 27, 2418–2447.

Miles, J.W., 1961. On the stability of heterogeneous shear flows. J. Fluid Mech. 10, 496–508.

Nakano, H., Suginohara, N., 2002. Effects of bottom boundary layer parameterization on reproducing deep and bottom waters in a world ocean model. J. Phys. Oceanogr. 32, 1209–1227.

Narimousa, S., Fernando, H.J.S., 1987. On the sheared density interface of an entraining stratified fluid. J. Fluid. Mech. 174, 1–22.

Ochoa, J., Bray, N.A., 1991. Water mass exchange in the Gulf of Cadiz. Deep-Sea Res. 38 (Suppl. 1), S465–S503.

Özgökmen, T.M., Fischer, P.F., Duan, J., Iliescu, T., 2004a. Three-dimensional turbulent bottom density currents from a high-order nonhydrostatic spectral element model. J. Phys. Oceanogr 34 (9), 2006–2026.

Özgökmen, T.M., Fischer, P.F., Duan, J., Iliescu, T., 2004b. Entrainment in bottom gravity currents over complex topography from three-dimensional nonhydrostatic simulations. Geophys. Res. Lett. 31, L13212. doi:10.1029/2004GL020186.

Özgökmen, T.M., Fischer, P., Johns, W.E., 2006. Product water mass formation by turbulent density currents from a high-order nonhydrostatic spectral element model. Ocean Model. 12, 237–267.

Papadakis, M.P., Chassignet, E.P., Hallberg, R.W., 2003. Numerical simulations of the Mediterranean Sea outflow: Impact of the entrainment parameterization in an isopycnic coordinate model. Ocean Model. 5, 325–356.

Peters, H., Johns, W.E., 2005. Mixing and entrainment in the Red Sea outflow plume. Part II: Turbulence characteristics. J. Phys. Oceanogr. 35, 584–600.

Peters, H., Gregg, M.C., Toole, J.M., 1988. On the parameterization of equatorial turbulence. J. Geophys. Res. 93, 1199–1218.

Peters, H., Johns, W.E., Bower, A.S., Fratantoni, D.M., 2005. Mixing and entrainment in the Red Sea outflow plume. Part I: Plume structure. J. Phys. Oceanogr. 35, 569–583.

Price, J.F., 2004. A process study of the Faroe Bank Channel overflow. Geophys Res. Abstr. 6, 07788.

Price, J.F., Baringer, M.O., 1994. Outflows and deep water production by marginal seas. Prog. Oceanogr. 33, 161–200.

Rohr, J.J., Itsweire, E.C., Helland, K.N., Atta, C.W.V., 1988. Growth and decay of turbulence in stably stratified shear flow. J. Fluid Mech. 195, 77–111.

Schlitzer, R., 2003. Ocean Data View, http://www.awi-bremerhaven.de/ GEO/ODV.

Serra, N., Ambar, I., 2002. Eddy generation in the Mediterranean undercurrent. Deep-Sea Res. II 49, 4225–4243.

Tufo, H.M., Fischer, P.F., 1999. Terascale spectral element algorithms and implementations, gordon bell prize submission. In: Proceedings of the ACM/IEEE SC99. Conference on High Performance Networking and Computing (CDROM). IEEE Computer Society.

Turner, J.S., 1986. The development of the entrainment assumption and its application to geophysical flows. J. Fluid Mech. 173, 431–471.

Wang, D., Large, W.G., McWilliams, J.C., 1996. Diurnal cycling, eddy viscosity and horizontal rotation effects in equatorial ocean boundary layers. J. Geophys. Res. 101, 3649–3662.

Wang, D., McWilliams, J.C., Large, W.G., 1998. Large eddy simulations of the diurnal cycle of deep equatorial turbulence. J. Phys. Oceanogr. 28, 129–148.

Wesson, J.C., Gregg, M.C., 1994. Mixing at Camarinal Sill in the Strait of Gibraltar. J. Geophys. Res. 99, 9847–9878.

Willebrand, J., Barnier, B., Böning, C., Dieterich, C., Killworth, P.D., Provost, C.L., Jia, Y., Molines, J., New, A.L., 2001. Circulation characteristics in three eddy-permitting models of the North Atlantic. Prog. Oceanogr. 48, 123–161.

Winton, M., Hallberg, R., Gnanadesikan, A., 1998. Simulation of density-driven frictional downslope flow in z-coordinate ocean models. J. Phys. Oceanogr. 28, 2163–2174.